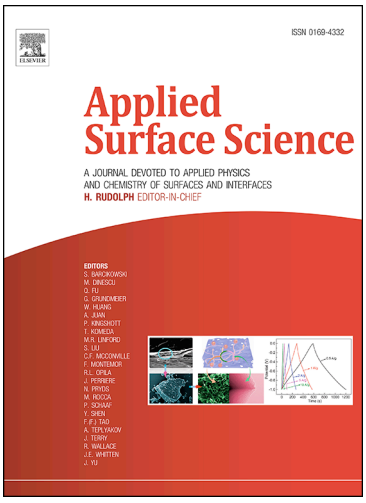

Full Length Article

Crumpled sheet like graphene based WO_3-Fe_2O_3 nanocomposites for enhanced charge transfer and solar photocatalysts for environmental remediation

A. Priyadharsan, V. Vasanthakumar, S. Shanavas, S. Karthikeyan, P.M. Anbarasan

PII: S0169-4332(18)33208-2
DOI: https://doi.org/10.1016/j.apsusc.2018.11.130
Reference: APSUSC 40976

To appear in: *Applied Surface Science*

Received Date: 18 July 2018
Revised Date: 9 November 2018
Accepted Date: 15 November 2018

Please cite this article as: A. Priyadharsan, V. Vasanthakumar, S. Shanavas, S. Karthikeyan, P.M. Anbarasan, Crumpled sheet like graphene based WO_3-Fe_2O_3 nanocomposites for enhanced charge transfer and solar photocatalysts for environmental remediation, *Applied Surface Science* (2018), doi: https://doi.org/10.1016/j.apsusc.2018.11.130

Crumpled sheet like graphene based WO_3-Fe_2O_3 nanocomposites for enhanced charge transfer and solar photocatalysts for environmental remediation

A. Priyadharsan,[a] V. Vasanthakumar,[b‡] S. Shanavas,[a‡] S. Karthikeyan,[c] P. M. Anbarasan,*[a]

[a]*Nano and Hybrid Materials Laboratory, Department of Physics, Periyar University, Salem 636 011, Tamil Nadu, India.*

[b]*Advanced Materials Chemistry Laboratory, Department of Chemistry, Periyar University, Salem 636 011, Tamil Nadu, India.*

[c]*Aston Institute of Materials Research (AIMR), Aston University, West Midlands B4 7ET, United Kingdom.*

[‡]*These authors made equal contributions to this work.*

**To whom correspondence should be addressed, e-mail: profpmanbarasan@gmail.com*

Fax: +91 427 2345124

Abstract

The combination of two or more metal oxides onto graphene sheets with even distribution is projected to enhanced charge transfer properties in photocatalytic applications. We report, tungsten oxide (WO_3) with iron oxide (Fe_2O_3) nanoparticles grown on graphene sheets via a facile economical one pot hydrothermal method and consequently characterized by standard analytical techniques. Synthesized Fe_2O_3 with WO_3 nanoparticles were well ornamented on surface of the graphene sheets which have a significant charge transfer properties. The resulting hybrid WO_3-Fe_2O_3-rGO (WFG) nanocomposites showed enhanced photocatalytic, heavy metal removal and antibacterial activities. The superior photocatalytic removal efficiencies were observed for the removal of rhodamine B (~94%) and methylene blue dyes (~98%) under solar light irradiation. The antibacterial activity of WFG nanocomposites were performed against *Escherichia coli* (*E.coli*) and *Staphylococcus aureus* (*S.aureus*) as models for Gram-negative and Gram-positive bacteria. The outcome of the results have an intellectual effect on the use of WFG nanocomposites to address the upcoming energy and environment issues.

Keywords: WFG nanocomposites; photocatalyst; antibacterial activity; dyes removal.

1. Introduction

The removal of highly colored wastewater especially, secondary effluent contains refractory organics from hazardous industrial chemicals is of great interest and significance for environmental protection [1]. The industrial generated wastewater contains residual organic compounds and dyes which posed adverse effect to human health [2,3]. Several advanced techniques have been used to deal with this serious phenomenon, such as biological, wet catalytic oxidation, ozonation, electrochemical, sonocatalytic, photochemical techniques, etc., [4,5] were used to remove organics from wastewaters, but still have challenge to complete elimination of this refractory organics [6]. Recently, photocatalytic processes are used as to remove refractory organics into smaller non-toxic organic molecules without sludge generation (i.e., secondary heavy metal pollution) by simple, efficient and an economical, to clean industrial effluent [7–9]. Numerous research on photocatalysis for wastewater containing organic and inorganic contaminants have been reported earlier [3]. Currently, inorganic heavy metals such as lead, cadmium and mercury are the environmentally significant pollutants and are flattering one of the most serious environmental threat. Thus, the removal of toxic heavy metals from industrial wastes is an important challenge to avoid water and soil pollution [10].

Semiconducting nanoparticles have drawn tremendous attention due to their unique physicochemical properties and potential applications in photocatalysis, solar energy production, energy conversion, carbondioxide reduction and supercapacitors [11,12]. Among numerous exposed photocatalysts, tungsten oxide (WO_3) and iron oxide (Fe_2O_3) nanoparticles were extensively studied for gas sensing, catalysis and solar energy conversion processes, and electrochromic displays, because of their economical and distinctive properties such as strong oxidizing abilities for superior conductivity, chemical stability, plasmon-resonant properties and

fine chemical production [13–16]. Fe_2O_3 nanoparticles have already been utilized by food and drug administration (FDA) of United States for food and medicinal applications [17]. It has been progressively used in the field of photocatalysis, due to high absorption in the visible region which is about 43 % in solar spectrum [18].

In this context, a number of binary photocatalysts such as, WO_3-Fe_2O_3 nanocomposite [19], WO_3-Fe_2O_3 nanosheet arrays [20] and Fe_2O_3@WO_3 nanostructures [21] were developed to recognize the reminiscence of photocatalysts by taking advantage of Fe_2O_3 magnetic properties. However, these binary composites always endure a poor photocatalytic efficiency after many cycles, [20] due to the chemical instability of Fe_2O_3 convinced by the photogenerated electrons moved from WO_3. In this regard, it is essential to enhance the stability as well as charge transport properties of the recollectable photocatalysts for practical use [22].

In recent years, many researchers have focused on several ways to improve the efficiency of photocatalysts, such as carbon, N-doping on WO_3/TiO_2, α-Fe_2O_3/graphene oxide, WO_3@graphene composite, and Cu_2O/graphene/α-Fe_2O_3 nanotube [23–26] among which graphene has showed excellent activity. Graphene has initiated new research area in material science, due to its unique sp^2 monolayer structure, remarkably high conductivity, superior electron mobility, enormously high specific surface area and chemical stability [27]. It is treated to be an ideal matrix and electron mediator of semiconductor nanoparticles for energy and environmental applications [28,29]. On the other hand, combinations of metal nanocomposites with graphene were attractive in improving photocatalytic activity under visible-light irradiation. Use of graphene/$BiVO_4/TiO_2$ nanocomposite, Ag/RGO/ZnO, Ag-Cu_2O/rGO and graphene oxide–$CuFe_2O_4$–ZnO nanocomposites as photocatalysts for environmental remediation have

been reported [30–33]. In specific, reduced graphene oxide (rGO) based ternary nanocomposites have great superiority than binary composites when used as photocatalysts.

On the other hand, antibiotic resistance is a severe and growing phenomenon in human health. Notably antibiotic resistant bacterial strains, fungi and parasites have become a serious problem for health care and food technology zones [34]. Thus, antibiotics having a different mechanism of action are instantly needed for changes in the traditional antimicrobial compounds. Because of their large specific surface area and high bioactivity, the improvements of nanoparticles with antimicrobial activity have been developed as a new class of biomedical materials having enhanced or distinct antibacterial activity against multi drug resistant human pathogenic microbes to fulfil cumulative demands for hygiene in daily life [35].

Herein, we report a simple hydrothermal method to prepare ternary graphene-semiconductor-magnetic nanocomposite, precisely referring to WO_3-Fe_2O_3-rGO (WFG) [22], which retains the combined functions as showed in Scheme. 1. The synthesized ternary WFG nanocomposites exhibited superior visible-light photocatalytic activity towards the degradation of two organic dyes, called methylene blue (MB) and rhodamine B (RhB) in synthetic waste water. The proposed mechanisms of the photocatalyst for WFG nanocomposites were discussed by relating with experimental details. The WFG nanocomposites were further investigated for antibacterial activity against *Escherichia coli* and *Staphylococcus aureus*. The developed material showed superior photocatalytic and antimicrobial properties. This synthesized photocatalytic material may afford significant antibacterial performance in environmental purification application.

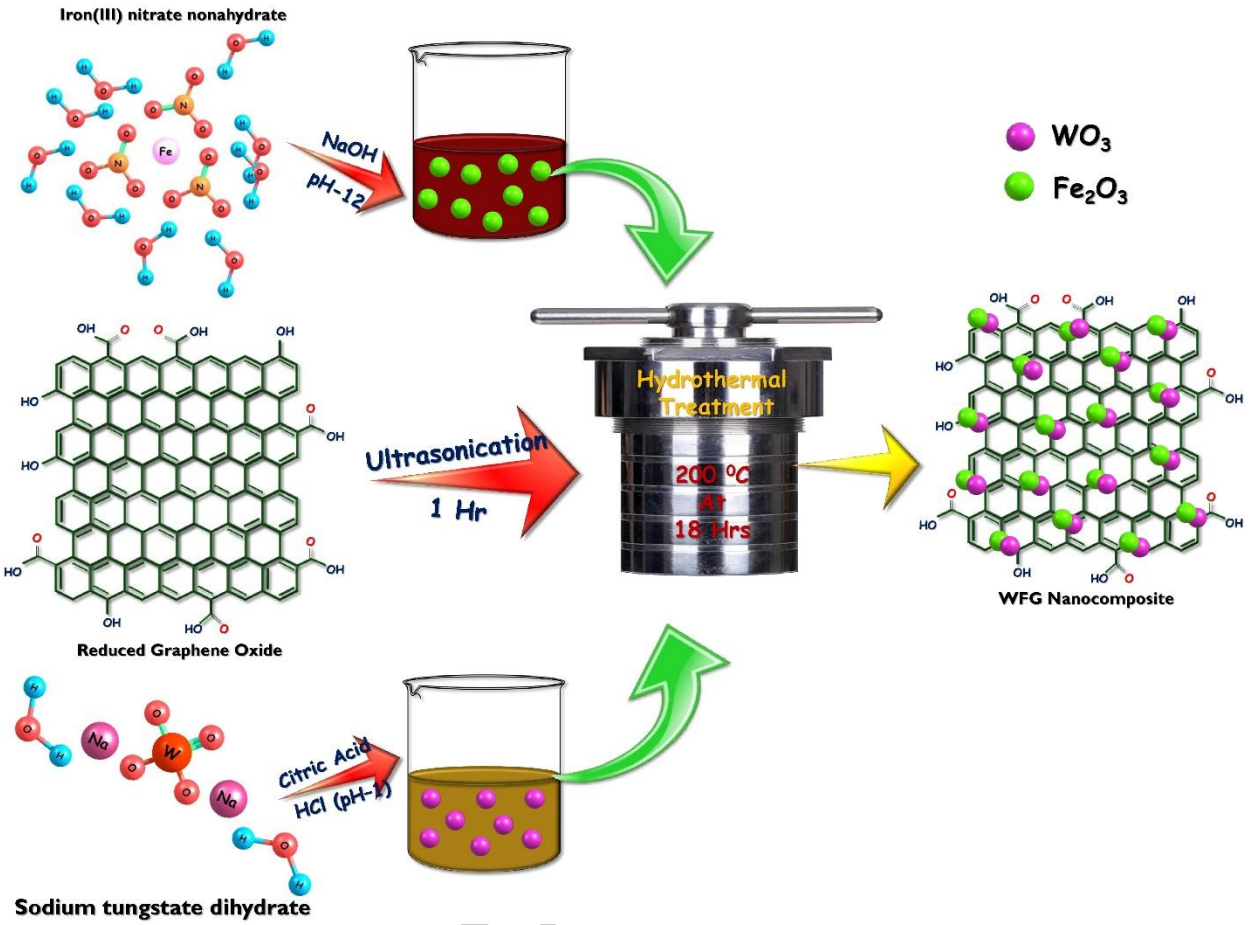

Scheme. 1. Schematic diagram for preparation of WFG nanocomposites

2. Materials and Methods

2.1 Materials and Reagents

Graphite powders, sodium tungstate dihydrate ($Na_2WO_4 \cdot 2H_2O$), ferric nitrate ($Fe(NO_3)_3 \cdot 9H_2O$) and sodium hydroxide (NaOH) were purchased from Sigma-Aldrich Co. Potassium permanganate ($KMnO_4$), hydrochloric acid (HCl), sulfuric acid (H_2SO_4) and hydrogen peroxide (H_2O_2), methylene blue dye, rhodamine B, working and standard metal ions solution were all purchased from Merck Chemicals, India. All the reagents and chemicals were used without any further purification.

2.2 Preparation of the WO_3-Fe_2O_3-rGO nanocomposites

Graphene oxide was synthesized through a modified Hummer's method [22]. WFG was synthesized by simple hydrothermal process. In a typical process, 0.30 g of rGO was added to 30 mL distilled water and then ultra-sonicated for 1 h. Then the rGO suspension was added 30 mL to aqueous solutions of $Na_2WO_4 \cdot 2H_2O$ (2.638 g), $Fe(NO_3)_3 \cdot 9H_2O$ (3.232 g) with continuous stirring. After 30 min reaction, the above mixture was transferred to a 100 mL Teflon-lined stainless-steel autoclave and heated at 170 $^{\circ}$C for 15 h. The obtained precipitate was separated by centrifugation and washed with ethanol and distilled water for several times. The resulting solid was dried in vacuum oven at 60 $^{\circ}$C over-night prior to characterization. For comparison, Pure WO_3, Fe_2O_3 and binary WO_3/rGO, Fe_2O_3/rGO nanocomposites were obtained through a similar procedure.

2.3 Characterization

The crystal structure of the products were carried out using a Rigaku Miniflex X-ray diffractometer with Cu Kα (λ = 0.15406 nm). Fourier transform infrared (FT-IR) spectra were recorded on a BRUCKER TENSOR 27 FTIR spectrophotometer. Raman spectra were recorded using a LabRAM HR Horbia Micro Raman spectrometer. The scanning electron microscope (SEM, Zeiss18 Evaluation) was employed to investigate the morphology and Energy dispersive X-ray spectroscopy (EDX Oxford X-Act) was used to find the elements composition. High resolution electron microscopy (HRTEM) and selected area electron diffraction (SAED) were measured on a Jeol/JEM 2100 transmission electron microscope operating at 200 kV. UV–vis Diffuse reflectance spectra (UV–vis DRS) were recorded in the range 200–800 nm with a Perkin Elmer Lambda 25 spectrometers.

The determination of Pb^{2+}, Cd^{2+} and Hg^{2+} concentrations was carried out on an ICP-OES using a Perkin Elmer Optima™ 7000 DV dual view series sequential spectrometer (Shelton, CT,

USA) equipped with WinLab™32 for ICP Version 4.0 software. In order to avoid any carry-over effects, the ultrasonic nebulizer was washed out with 1% (v/v) HNO_3 for 60 s between each sample run. Argon gas (99.99%) was used as the ICP torch gas and nitrogen gas was used as the optical purge gas. A charge-coupled device (CCD)-array detector was used to collect both the analyte spectra and the background spectra, which provided improved precision and analytical speed. The three analytical emission wavelengths of 220.353, 228.802 and 253.652 nm were employed for quantification of Pb, Cd and Hg. The repeatability was calculated for ICP-OES as the relative standard deviation (RSD) on six consecutive replicates of the same sample.

2.4 Evaluation of Photocatalytic activity

The MB and RhB were chosen as a model organic pollutants to test the photocatalytic activity of WFG photocatalyst at room temperature. A typical reaction mixture for irradiation comprised the following initial concentrations: 100 mg of the prepared samples were added to 100 mL of different dye solutions (30 mg/mL). Prior to the photocatalytic activity testing, the reaction mixture was kept for 30 min in a dark environment to establish the adsorption/desorption equilibrium of the dye molecules on the photocatalyst surface. The mixture then continuously irradiated with 450 W low pressure quartz mercury lamp for 1 h. The suspension was periodically withdrawn from the reactor, and the samples were then centrifuged to remove the photocatalyst powder. The photocatalytic activity of the samples was calculated from initial and final reaction mixture containing MB and RhB by time using UV–vis spectrophotometer. As for the stability test, the remaining photocatalyst powder was centrifuged and used upto 4 cycles for photocatalytic degradation efficiency of WFG towards MB and RhB. For comparison, the auto photodegradation of MB and RhB (namely, photolysis) were also tested under similar conditions in the absence of photocatalyst. The photocatalytic degradation

efficiency of WFG on degradation of MB and RhB were evaluated by the value of C/C_0, where C_0 and C are the symbolic representations for the concentration of organic pollutants before and after photocatalytic experiments, respectively.

2.5 Metal ion adsorption properties of WFG ternary nanocomposites

2.5.1 Removal of toxic metal ions at different pHs

The heavy metals removal capacity of the prepared WFG nanocomposites were studied by batch equilibrium method. Briefly, Dried 0.5 g of WFG nanocomposites was added to 300 ppm (100 mL) solution of mixture of Pb^{2+}, Cd^{2+} and Hg^{2+} metal ions, pH was maintained as 2, 3, 4, 5, 6 and 7 by using 0.5 M HCl or 0.5 M NaOH aqueous solutions at 25 ± 0.5 ^{o}C with continuous stirring of 200 rpm for 12 h to facilitate the adsorption equilibrium of heavy metals onto the WFG nanocomposites. After the specified time, the WFG nanocomposites were separated out from the solution by filtration through Whatman filter paper (No. 42). The filtrate were collected and then the amount of metal ions was determined by ICP-OES. A blank was also analyzed to ensure that no metal ions were carried over from the previous sample. The blank values were subtracted from the values determined for the different metal ions to give the exact adsorbed metal ion concentrations. The amount of metal ions removed by WFG nanocomposites in the presence of a given pH was calculated by following expression:

$$\% \text{ Removal efficiency} = C_o - C_e/C_o \times 100.$$

where, Co is the initial metal ion concentration (ppm), Ce the equilibrium metal ion concentration in ppm

2.6 Antibacterial Activity

2.6.1 Chemicals for antibacterial assay

Chloramphenicol (Hi-Media, Pvt Ltd., India) was used as a positive reference standard for selected two bacterial strains *E.coli* and *S.aureus*, respectively. 10% dimethyl sulfoxide (DMSO) (Qualigens) was used as a solvent for the tested samples.

2.6.2 Preparation of inoculums

Two different human pathogenic bacterial strains of gram positive bacteria and gram negative bacteria were used in our current study. The gram positive strain was *Staphylococcus aureus* while the gram negative bacteria was *Escherichia coli*. The tested bacterial species were obtained from microbial type culture collection centre, Chandigarh, India. Bacterial inoculums were prepared by growing freeze-dried cells in nutrient agar for 24 h at 37 ºC. WFG ternary nanocomposite was assessed for their antibacterial activity by agar modified well diffusion method using nutrient agar media [36]. The catalyst was dissolved separately in diluted 10% dimethyl sulfoxide. The catalyst was tested against *E. coli* and *S. aureus* at different concentrations (50, 75 and 100 µg/mL) and incubated at 37 °C for 24 h. The inoculums of two bacterial strains were prepared by suspending overnight grown cultures in normal saline (NaCl 0.85%). The turbidity of the inoculum was adjusted as per the 0.5 McFarland standards.

2.6.3 Agar well diffusion method

The antibacterial activity of WFG nanocomposite was investigated quantitatively through the different doses of materials supplemented in the growing media. For the antibacterial assay, WFG nanocomposites with different concentrations were filled in the wells. Dilute DMSO was used as a negative control and the standard drug, chloramphenicol was used as a positive control. After overnight incubation in the incubator at 37 °C, all plates were examined and the zone of inhibition (diameter) was measured. After incubation, the colony forming units (cfu) were counted in the respective dilutions of the treated sample.

3. Results and Discussion

3.1 Crystal structures

Powder XRD was used to examine the structural and crystal phases of the synthesized pure, binary and WFG ternary nanocomposites. The X-ray diffraction (XRD) pattern of WFG nanocomposites are presented in Fig. 1, which showed the major peaks corresponding to hexagonal WO_3 (JCPDS No. 85-2459) at 2θ values of 12.8° (1 0 0), 24.19° (0 0 2), 28.8° (2 0 0), 30.1° (1 1 2) , 34.8° (2 0 2), 36.5° (2 1 0), 38.1° (2 1 1), 45.8° (2 1 2), 50.1° (2 2 0), 52.6° (3 1 0), 55.4° (2 2 2), 59.5° (4 0 0), 64.7° (3 1 3) and 70.3° (2 2 4). The Fe_2O_3 (JCPDS No. 33-0664) at 24.2° (0 1 2), 33.2° (1 0 4), 35.7° (1 1 0), 40.9° (1 1 3), 49.5 (0 2 4), 54.1° (1 1 6), 57.6° (1 2 2), 62.5° (2 1 4), 64.1° (3 0 0), 72° (1 1 9) and 75.6° (2 2 0), and reduced graphene oxide at 24.52° (0 0 2) [37]. However, no rGO peak observed in the WFG nanocomposites, which is due to its low amount, highly dispersed and comparatively low diffraction intensities in the composites [38,39]. Also, the XED peak of WFG nanocomposites significantly shifting to high-angle, this reason can be explained the well bound between WO_3-Fe_2O_3 and the two composite interconnecting heterojunction with rGO, which results the semiconductors shrinkage in the lattice [40,41]. The diffraction spectra confirm the formation of the hexagonal crystalline phase of WO_3 and rhombohedral crystalline phase of Fe_2O_3 grown over the rGO sheet. Here, we showed that GO cannot be fully reduced into rGO during the synthesis process and therefore some of the oxygen based functional groups are often attached to rGO sheet even after the reduction [42]. The average crystallite size of the all samples were estimated using the Debye-Scherrer equation [43], which is presented in Table 1. The lattice parameters, degree of crystallinity and crystallite size of pure, binary and ternary nanocomposites were calculated and

provided in Table 1. The calculated d-spacing is in good agreement with HR-TEM of ternary nanocomposites.

Table 1. Lattice parameters, crystallite size and degree of crystallinity of pure, binary and ternary nanocomposites.

Sample	**Lattice Parameters (Å)**		**Crystalline size**	**Degree of crystallinity** (X_c)
	a = b	**c**	**(nm)**	
WO_3	7.147	7.754	51.20	3.221
Fe_2O_3	5.124	13.642	66.02	6.764
WO_3-rGO	7.148	7.755	72.97	8.990
Fe_2O_3-rGO	5.125	13.643	52.12	3.151
WFG	-		48.14	2.784

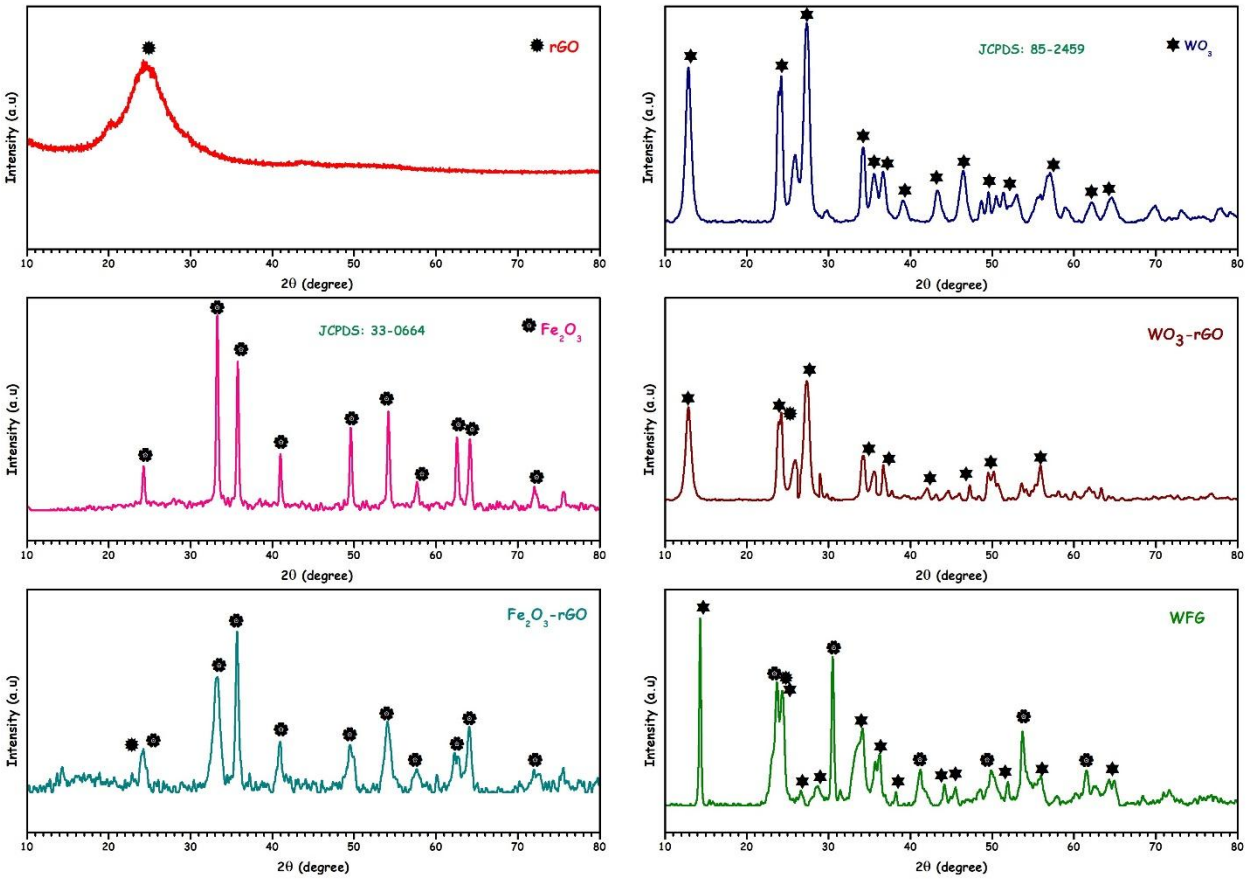

Fig. 1. Powder XRD patterns of pure, binary and WFG nanocomposites.

3.2 Morphology studies

FE-SEM and HR-TEM analysis of WFG was carried out to identify the morphology, particle size and structures. The morphology of rGO and WFG nanocomposites is presented in Fig. 2(a-e). Notably, the morphology of WFG nanocomposites greatly deviated, compared with a crumpled sheet like structure rGO (Fig. 2(a,b)). Moreover, WO_3 and Fe_2O_3 nanoparticles are randomly ornamented on rGO sheet surface, which could efficiently prevent the stacking of rGO sheets [44]. HR-TEM images of the pure WO_3 and Fe_2O_3 particles with sizes of different magnifications presented in Fig. S1(a-d). The HR-TEM images of WFG nanocomposites, where rGO exhibits wrinkled and folded sheets like structures showed in Fig. 3(a-f). The WO_3 and

Fe_2O_3 metal oxides nanoparticles (black in colour) are consistently disseminated on rGO sheets. Inset of Fig. 3f clearly describes the selected area electron diffraction (SAED) pattern of the ternary nanocomposites which showed that material is in polycrystalline nature. The (d_{002}) planar spacings of 0.43 nm corresponds to rGO layers [24,25]. While the (d_{020}) and (d_{110}) planar spacings of 0.38nm and 0.25 nm confirmed the plane of WO_3 and Fe_2O_3 (Fig. 3(c,f)) which is good agreement with XRD pattern. The EDX spectrum of WFG displays the only existence of C, O, Fe and W, indicating the successful formation of nanocomposite with high purity, which is analyzed by EDX and presented in Fig. 2f. The concentration elements (wt %) in this catalyst is listed in Fig. 2f.

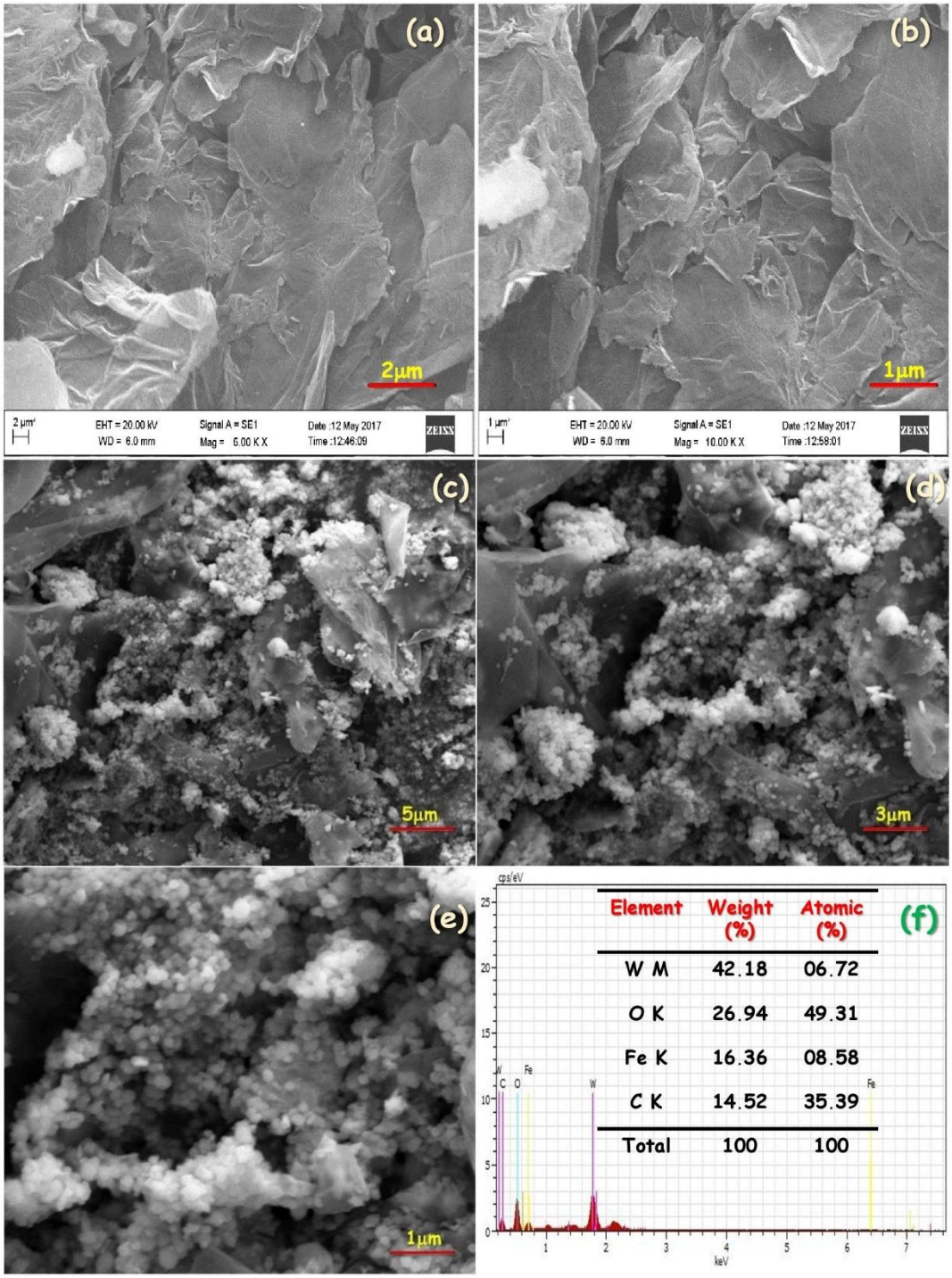

Fig. 2. FE-SEM images of rGO (a,b) and different magnifications (c-e) and EDX spectrum of WFG nanocomposites (f).

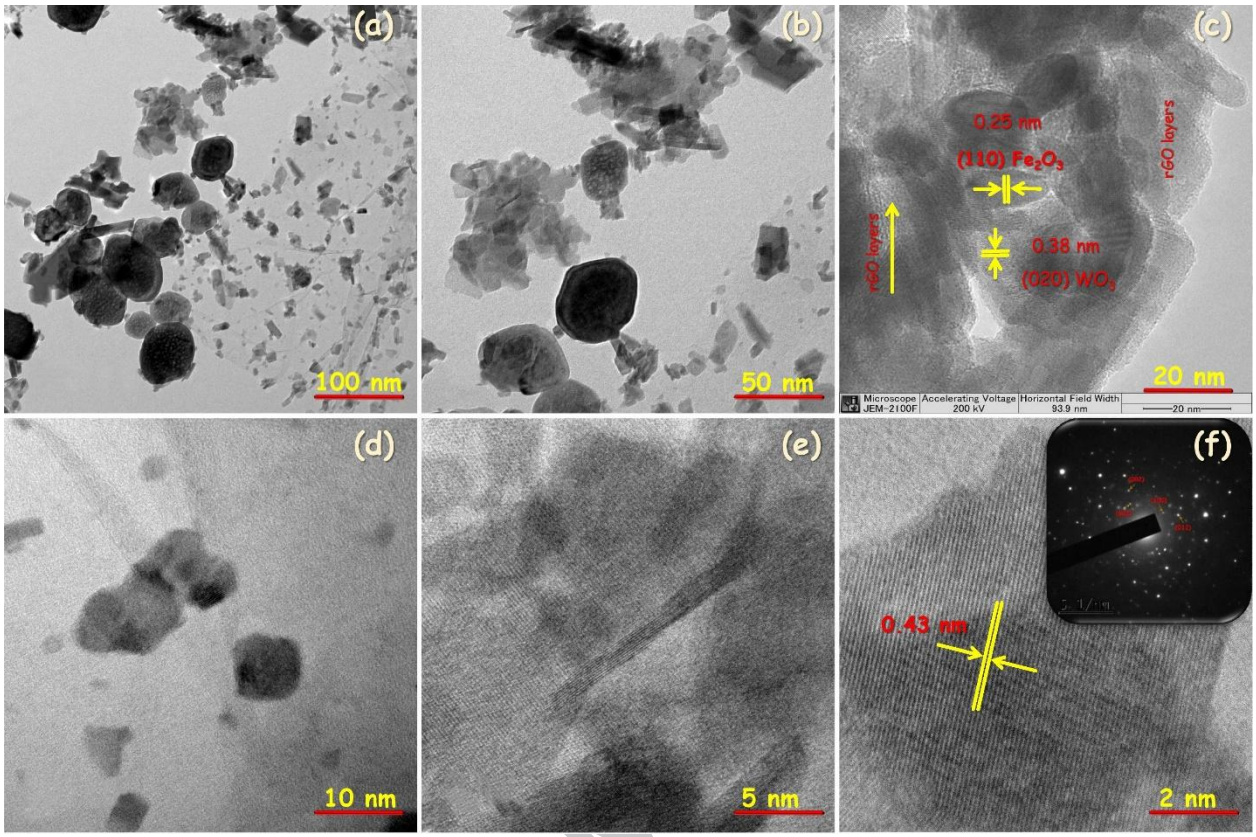

Fig. 3. (a-f) HR-TEM images of WFG different magnifications and (f) SAED patterns (insert: right corner) of WFG nanocomposites.

3.3. Surface chemical states/ properties by XPS

X-ray photoelectron spectroscopy was used to determine the chemical oxidation states of elements of WFG nanocomposites as presented in Fig. 4(a-e). Fig. 4a showed the XP survey spectrum of WFG nanocomposite confirmed W, Fe, C and O elements. From the survey XP spectra of C1s binding energy at 284.6 eV, O1s binding energy at 530.4 eV, W 4f binding energies at 35.4 eV and 37.5 eV, and Fe_2O_3 binding energy peaks at 724.32 eV, 710.72 eV (auger electron peak of Fe_2p) [45,46]. The deconvolution XP spectra of WO_3 (Fig. 4b), reveal the characteristic doublet binding energies at 35.4 eV and 37.5 eV for $W4f_{7/2}$ and $W4f_{5/2}$, respectively, which is good agreement with reports [47,48]. The deconvolution XP spectra of Fe_2O_3 (Fig. 4c), and the main characteristic binding energies at 710.72 eV and 724.32 eV,

corresponds to $Fe2p_{3/2}$ and $Fe2p_{1/2}$ spin-orbit peaks of Fe species in Fe_2O_3 which is in good agreement with reports [49,50]. The core level deconvolution C1s XP spectra (Fig. 4d) reveals the existence of O-C=O (290.84 eV), C–O (287.8 eV), and C-C 284.6 eV) functional groups, which responsible interaction between the nanocomposites. The core level O1s XP spectra was asymmetric and broad due to available multiple chemical environment in oxygen functionalities in WFG, and the binding energy at 530.4 eV and 529.4 eV is ascribed to WO_3 [49,51] and Fe_2O_3 [51], and binding energy at 531.8 eV corresponds surface chemisorbed oxygen functionalities [52,53].

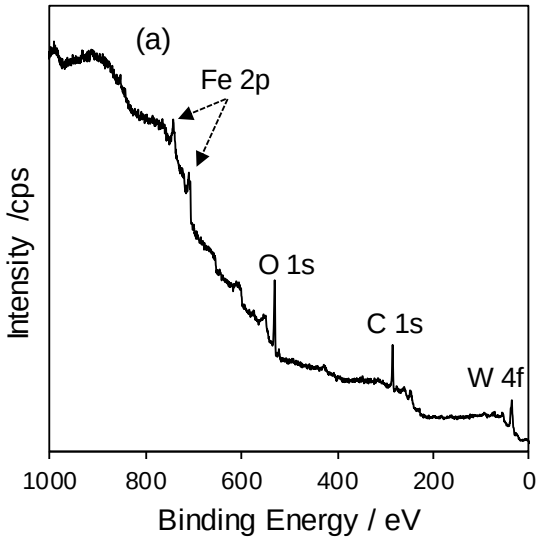

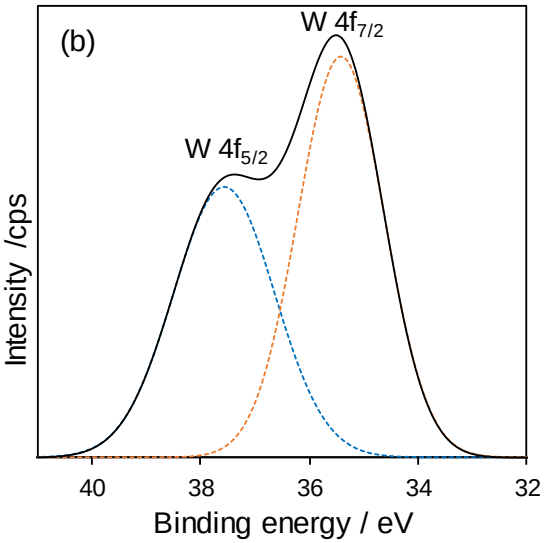

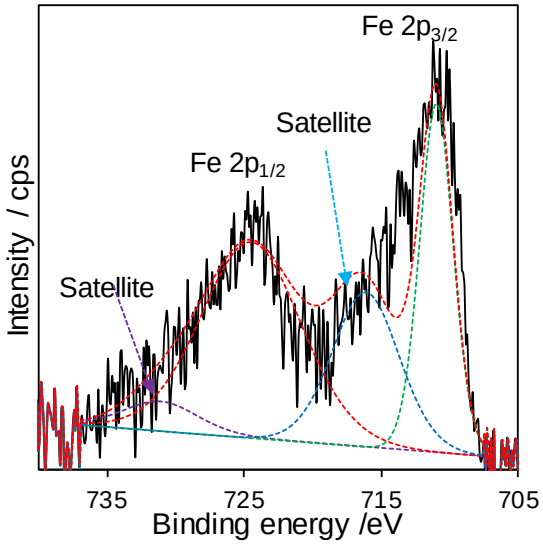

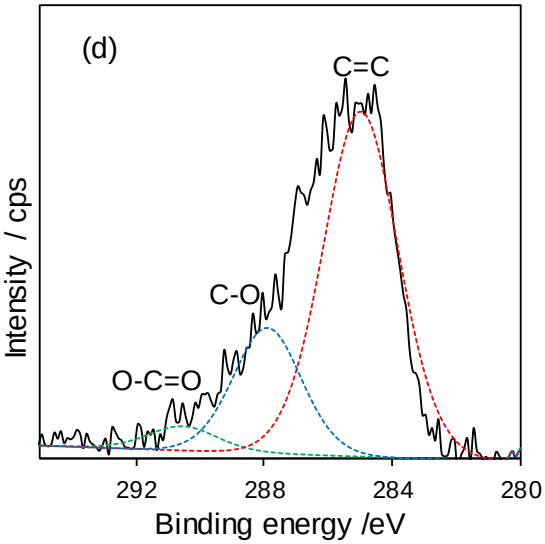

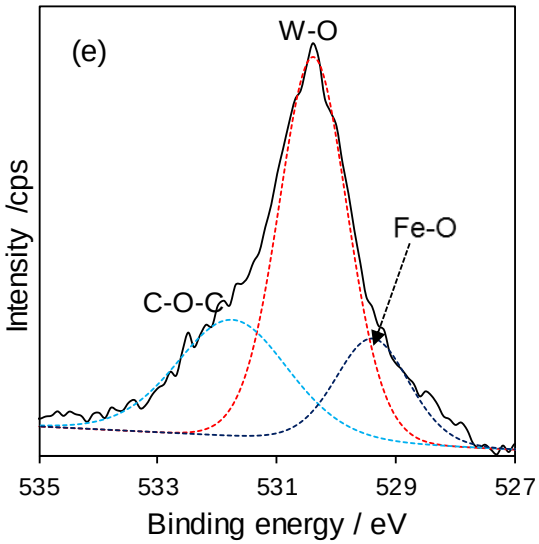

Fig. 4a. XPS results of the WFG nanocomposites, deconvolution XP spectra of W 4f (b), Fe 2p(c), C 1s(d) and O 1s(e).

3.4 Functional group Analysis

Fourier Transform Infrared Spectra (FT-IR) of as synthesized pure, binary and the WFG nanocomposites are presented in Fig. 5. In FT-IR spectrum of WFG, the broad peak around 3459 cm^{-1}, is attributed to stretching vibration of O-H of rGO with metal oxide interaction [53]. The weak adsorption band at 1581 cm^{-1}, is due to characteristic band of C=O functional groups in carbonyl and carboxyl moieties. The wide absorption band of WO_3-rGO nanocomposite at low frequencies is attributed to W-O-W bond. The peak at 1427 cm^{-1} confirmed the skeletal vibrations of unoxidized graphitic (C=C) domains [54]. Few functional groups have been vanished in ternary nanocomposites due to the hydrothermal treatment of precursor material. Furthermore,

The Raman spectra is most promising tool to determine metal and rGO. Fig. 6(a-c) showed Raman spectra of WO_3, Fe_2O_3, and WFG nanocomposites. The Raman bands of 250 cm^{-1}, 700 cm^{-1} assigned to O–W–O bending modes [55]. Fig. 6a showed the minor phonon confinement effects are perceived on the major phonon of 670 cm^{-1} assigned to O–W–O stretching mode and the 957 cm^{-1} assigned to WO_3 surface dangling bonds [56]. The Raman spectrum (Fig. 6b.) reveals the peaks at 223 and 487 cm^{-1} corresponds to A1g and the peaks at 242, 296, 336, 408, and 605 cm^{-1} corresponds to Eg vibrational modes of Fe_2O_3, good agreement with previous reports [57,58].

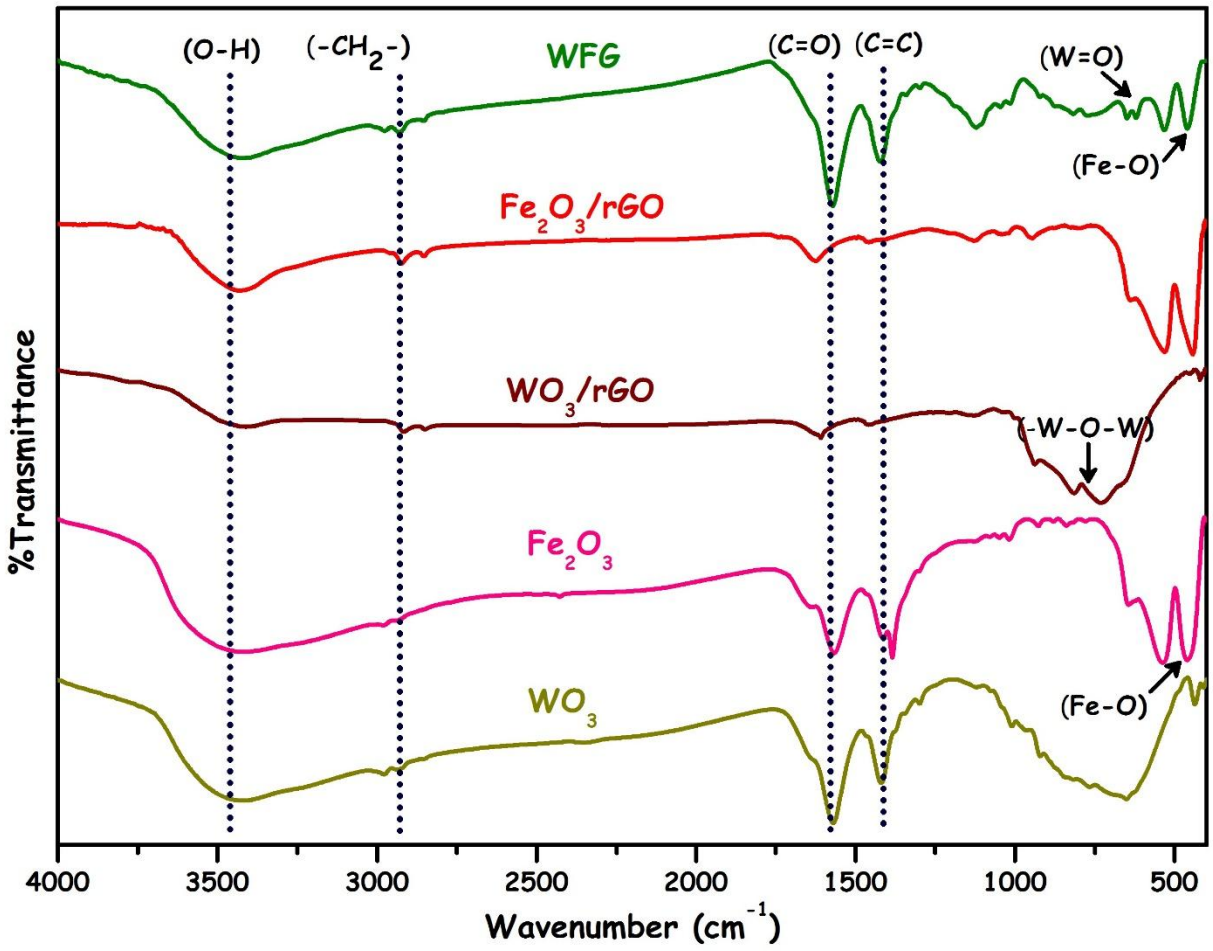

Fig. 5. FT-IR spectra of pure, binary and WFG nanocomposites

Fig. 6c showed that the two main peaks at 1324 cm^{-1} and 1567 cm^{-1} correspond to the characteristic sp^3 carbon (D band) and sp^2 bonded carbons (G band) of the rGO sheets [59]. These Raman results suggest the presence of electronic interaction between WO_3, Fe_2O_3 and rGO in the composite, thus confirming the successful incorporation of the WO_3 and Fe_2O_3 particles onto the rGO surface.

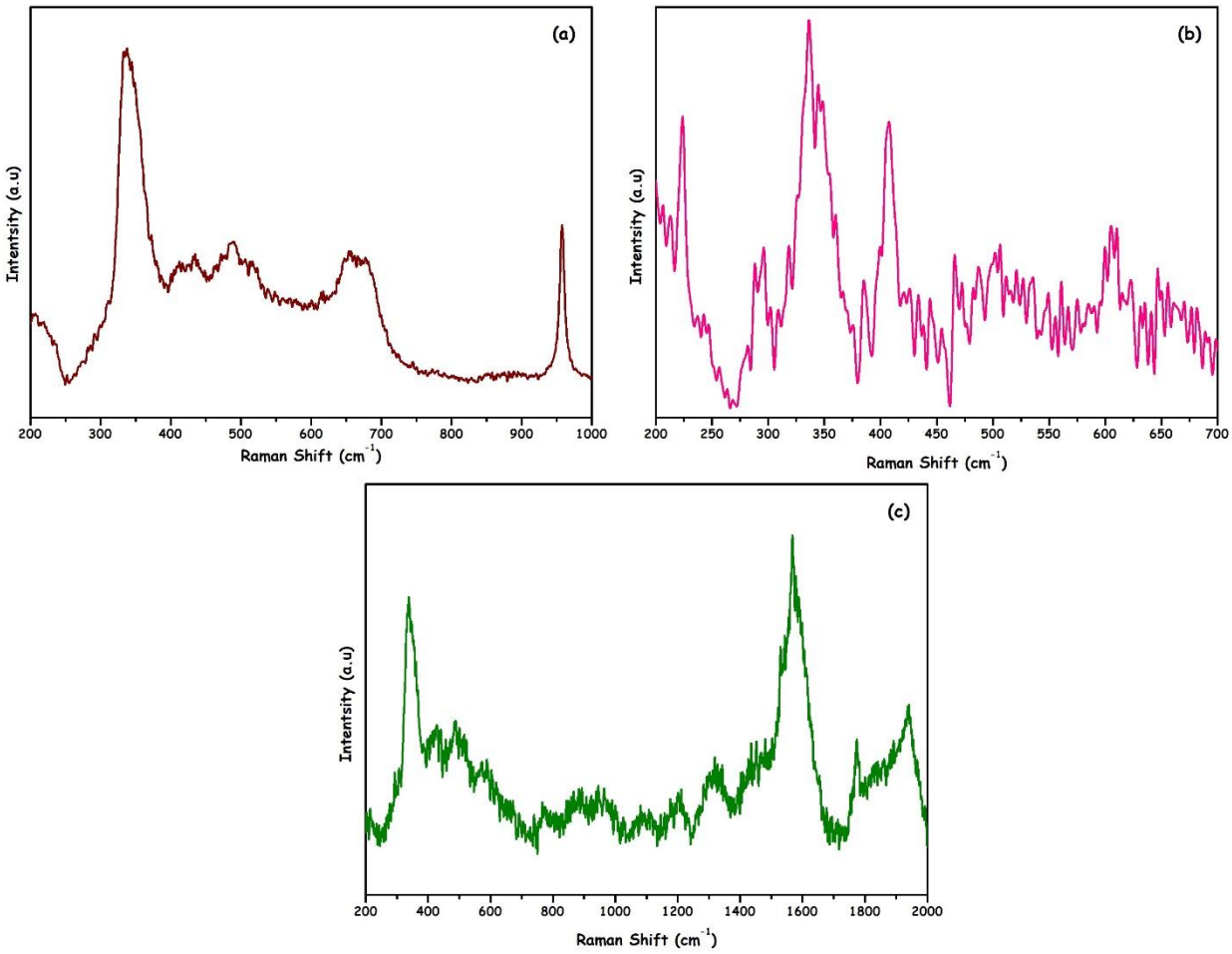

Fig. 6. Raman spectra of WO_3 (a), Fe_2O_3 (b), and WFG (c) nanocomposites

3.5 Optical and bandgap by UV–DRS spectroscopy

The optical absorption properties of WO_3, Fe_2O_3, WO_3/rGO, Fe_2O_3/rGO and WFG nanocomposites were studied by UV–DRS spectroscopy and corresponding absorption peaks are presented in Fig. 7. The absorption edge of all synthesized photocatalysts are exhibited at the range of ~450-600 nm. However, all composite samples produce a certain absorption intensity in the visible region. The band gap energy (Eg) of WO_3, Fe_2O_3, WO_3/rGO, Fe_2O_3/rGO and WFG nanocomposites (Fig. 7b) were calculated to be ~2.8, 2.33, 2.87, 2.63 and 2.73 eV respectively, according to the Kubelka-Munk method [22].

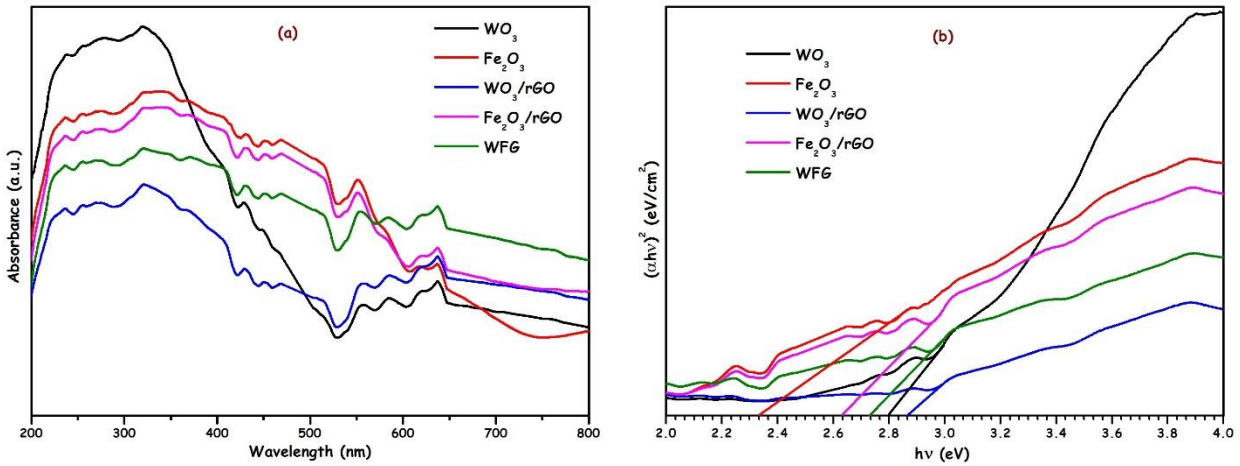

Fig. 7. (a) UV-vis spectra of pure, binary and WFG nanocomposites, (b) Tauc Plot of pure, binary and WFG nanocomposites

Pure WO_3 showed the light absorption in the UV range with absorption on-set at 450 nm. By comparing with all samples, WFG composites showed largely varied absorption in visible light region (450–800 nm), resulted from rGO introduction [9,22]. Though, the band gap width of Fe_2O_3 is figured out at 2.33 eV, while that of Fe_2O_3/rGO is 2.63 eV, as shown in Fig. 7b. The difference in the band gap broadening of Fe_2O_3 nanocomposites is due to the band structure aberrance induced by hetero-interfaces [60]. These interpretations also suggest that the presence of rGO indirectly changes functional process of electron-hole pair creation of WO_3 and Fe_2O_3 by increasing its surface electric charge in photochemical process [61].

3.6 Photocatalytic performance of Methylene Blue and Rhodamine B

Photocatalytic degradation of MB and RhB were carried out to found the catalytic performance of WFG nanocomposite under solar light irradiation. The photocatalytic removal efficiency of WFG on removal of MB and RhB were examined by UV-Vis spectra and compared with pure, binary and WFG ternary nanocomposites as shown in Fig. 8(a-c) and Fig. 9(a-c). Additionally, the photocatalytic removal rate of dyes (MB and RhB) of pure, binary and WFG ternary nanocomposite are presented in Fig. 8d and Fig. 9d. As illustrated in Fig. 8c and Fig. 9c,

the maximum absorption peaks of MB found at 664 nm and RhB at 554 nm, which is drastically decreased without shifting the peak position to the baseline, indicating that the dyes were completely eliminated/removed from the aqueous phase. However, the required reaction time is only 20 min for complete removal of MB and RhB dyes under solar light irradiation in the presence of WFG nanocomposite. It showed that the WFG nanocomposite has excellent solar light photocatalytic activity for the removal of MB at ~98% and RhB at ~94.5%, which is about ~3 times and ~1.4 times higher than that pure and binary photocatalysts. The optimum reaction time to removal of dyes was optimized as 20 min, and no marginal enhancement was found after 20 min reaction period.

The comparative photocatalytic activity of our photocatalyst with existing reports are presented in Table 3. The photocatalytic performance of the pure, binary and WFG nanocomposites were explored for MB and RhB removal under solar light irradiation, and expressed as the resulting degradation efficiency derived from UV-Vis analysis of the reaction mixtures.

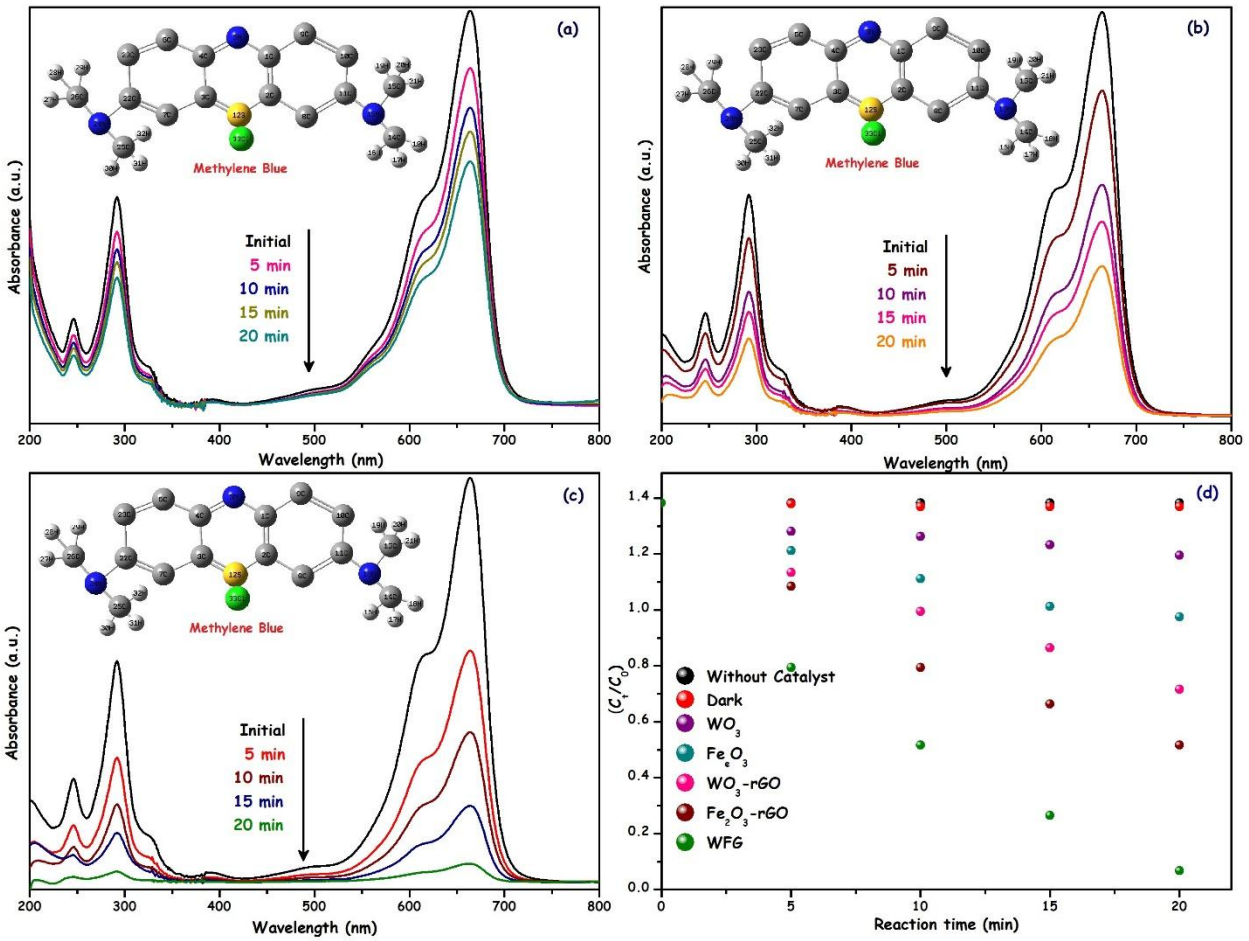

Fig. 8. UV–Vis spectra of MB at different time intervals: (a) WO_3-rGO, (b) Fe_2O_3-rGO, (c) WFG ternary nanocomposites and (d) MB removal rate at different photocatalytic system.

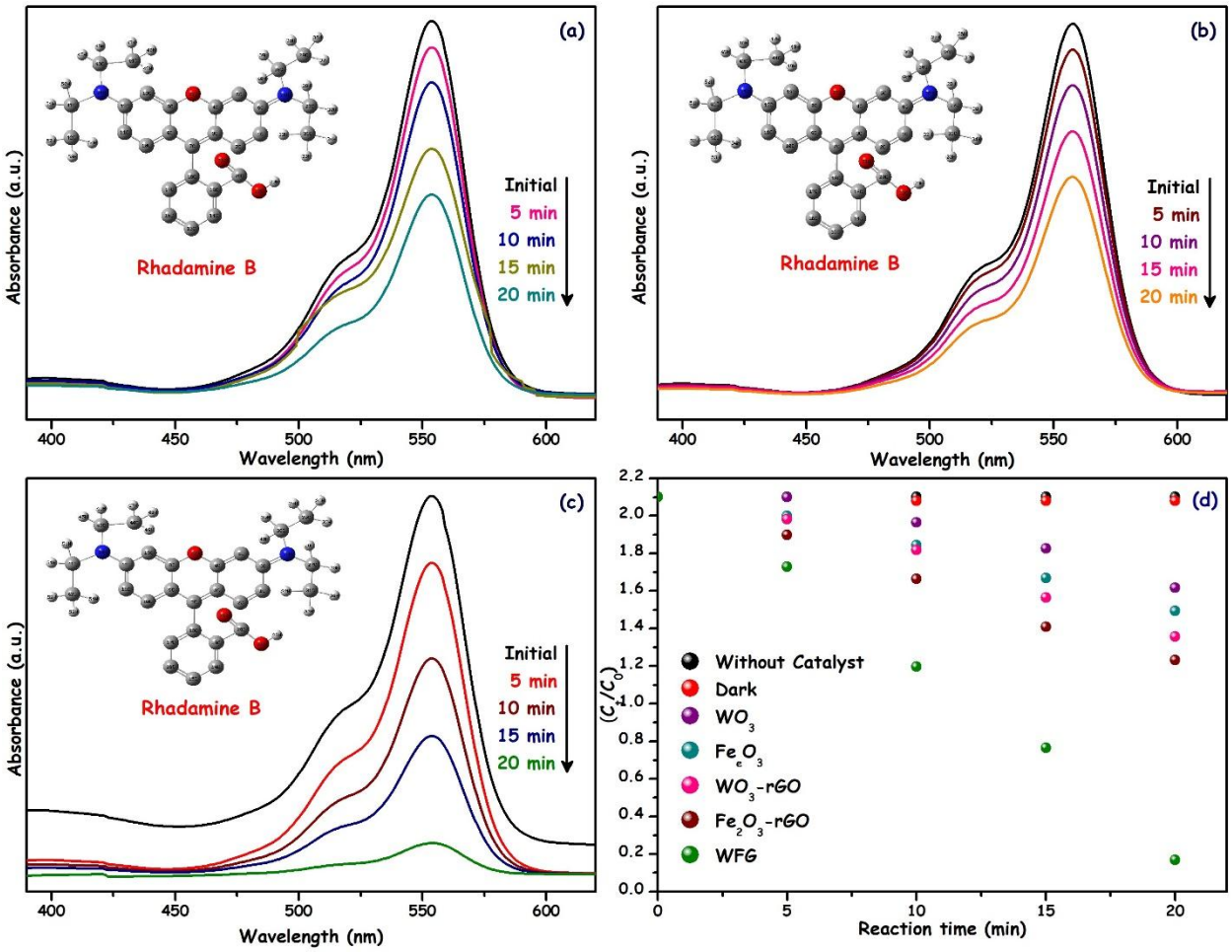

Fig. 9. UV–Vis spectra of RhB removal at different time intervals: (a) WO_3-rGO, (b) Fe_2O_3-rGO, (c) WFG ternary nanocomposites and (d) RhB removal rate at different photocatalytic system.

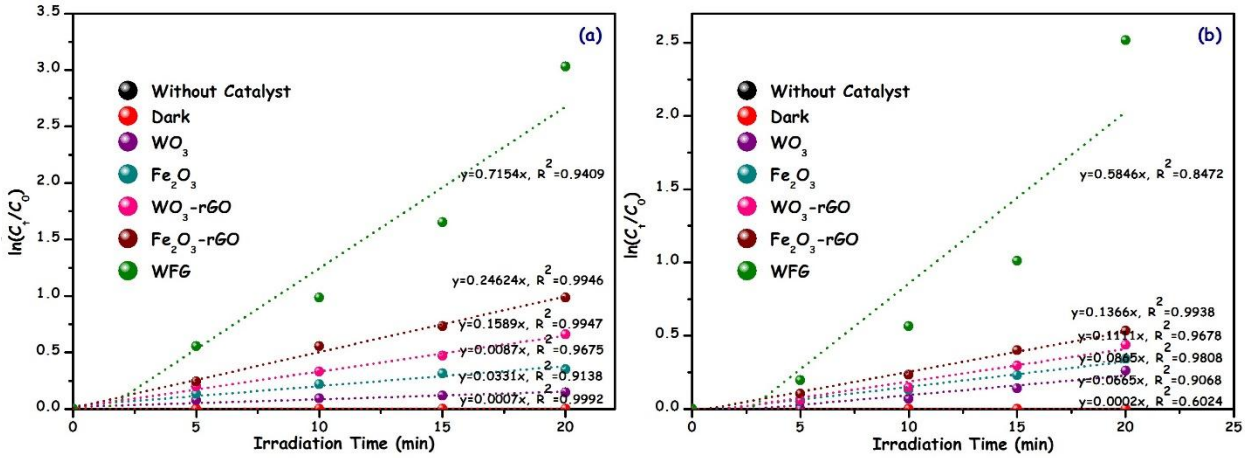

Fig. 10. Pseudo-first-order kinetics for photocatalytic degradation of (a) MB and (b) RhB by pure, binary and WFG catalyst

The photocatalytic degradation of MB and RhB rates were fitted with pseudo-first-order kinetics as presented in Fig. 10(a,b). The rate constants were determined according to the following equation (1) [62]

$$\ln(C_0/C_t) = kt \quad (1)$$

where, C_0 is the initial concentration, C_t is the concentration of MB and RhB dyes at varied time t, t referred irradiation time and k rate constant, which is derived from MB (absorption maxima at 664 nm) and RhB (absorption maxima at 554 nm) with respect to time. The reaction rate constants (k) for all photocatalysts were determined from slope of fitted curves and rates are provided in Table 2. All the plots showed a linear association with good correlation coefficients (R^2=0.9409 and R^2=8472), indicating that MB and RhB degradation using the synthesized catalysts under solar light irradiation, and it is confirmed that the highest removal rates (k, 0.7154 min^{-1} and 0.5846 min^{-1}) were obtained for WFG ternary nanocomposite.

Table 2. MB and RhB removal percentage and rate constant for different photocatalyst

Photocatalyst	**Degradation (%)**		***k* (min^{-1})**		***R^2***	
	MB	**RhB**	**MB**	**RhB**	**MB**	**RhB**
WO_3	13.60	23.08	0.0331	0.0665	0.9138	0.9068
Fe_2O_3	29.51	28.98	0.0087	0.0865	0.9675	0.9808
WO_3-rGO	48.23	35.45	0.1589	0.1111	0.9947	0.9678
Fe_2O_3-rGO	62.69	41.35	0.2462	0.1366	0.9946	0.9938
WFG	97.61	93.92	0.7154	0.5846	0.9409	0.8472

In this photocatalyst experiments, rGO acted as an acceptor in WFG nanocomposites, and subsequently reduced the charge recombination in the photocatalytic system. The difference

might be the presence of rGO, which contributed to charge transfer [27]. For a traditional semiconductor photocatalyst, both electrons and holes generated in the photocatalyst could decompose pollutants directly. Alternatively, electrons could also react with oxygen to produce oxy radicals, which finally convert into hydrogen peroxide. In this case, holes would react with hydroxyl ions to produce hydroxyl radicals. Hydroxyl radicals are the most active species to decompose pollutants in the photodegradation process [63]. In our experiments, rGO could act as an acceptor of the electrons generated in WO_3 and Fe_2O_3 nanoparticles, supposedly suppressing the recombination of charges and enhancing the photocatalytic activity. As to the reactive oxy radicals, we believe they may be generated on the surface of rGO as electrons have been efficiently transferred onto rGO. As the reactive oxy radicals, may create free electrons on the surface of rGO could transferred onto metal oxide surface. WFG nanocomposites formed in the hydrothermal route can effectually enrich the transfer efficacy of excited electrons and obstruct the recombination of electron-hole pairs, endowing the photocatalyst with enhanced solar light photocatalytic activity [64].

The possibility of hydroxyl radical influenced in our photocatalytic system, which is confirm the generation of $^{\bullet}OH$ radicals during the reaction. Electron paramagnetic resonance (EPR) studies, DMPO radical trapping experiments confirmed the hydroxyl radical formation over graphene based WO_3-Fe_2O_3 nanocomposites with model pollutant (MB dye) were presented in Fig. 11. From the Fig. 11. its evidenced the formation of DMPO-$^{\bullet}OH$ which is characteristic of hydroxyl ($^{\bullet}OH$) radicals generated during the photodegradation experiment compared with standard DMPO [65,66].

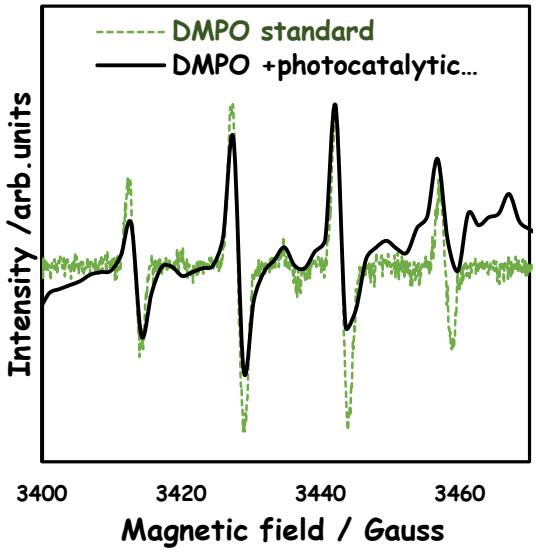

Fig. 11. EPR spin trapping experiments over WFG nanocomposites (Experimental conditions: MB; 30 mg/L, WFG; 100 mg /100mL and reaction time: 25 min)

Apart from the photocatalytic activity, the stability is also predominant significance for its supportable recyclability [67]. Fig. 12(a,b) displays the recycling tests for the degradation of MB and RhB dyes over WFG nanocomposites under solar light irradiation, which confirmed that no noticeable loss in photocatalytic activity was perceived after four consecutive recycles, therefore suggesting that the WFG nanocomposite has best photostability.

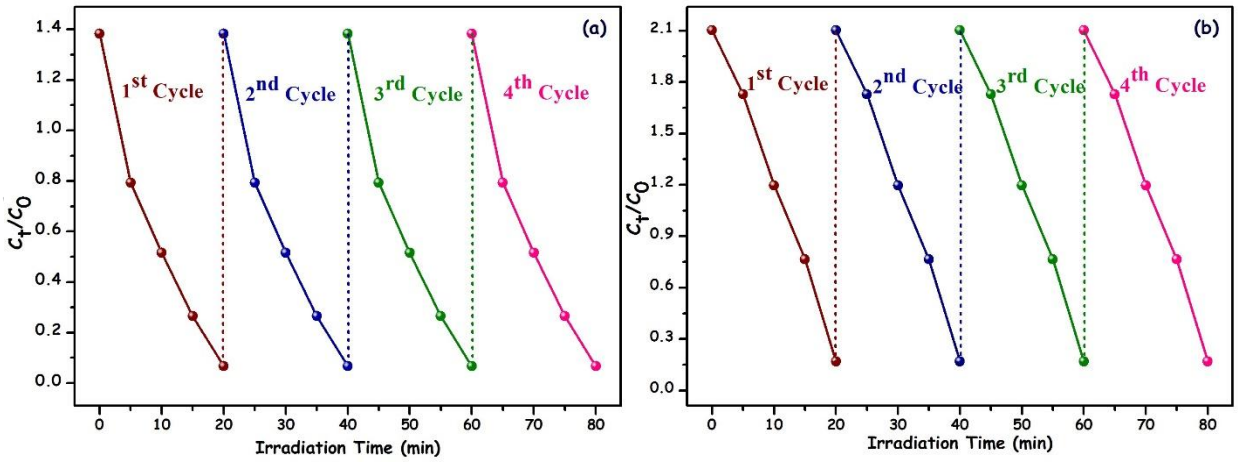

Fig. 12. Stack plots showing % degradation of (a) MB vs time and (b) RhB vs time for WFG nanocomposite at different cycles.

3.6.1 Possible photocatalytic mechanism

On the basis of above discussion, it is well known that there are numerous factors played in photocatalytic activity of metal oxide semiconductors: crystal structure, charge separation efficiency, and so on. The enhanced photocatalytic performance of WFG nanocomposite is attributed to combined interaction and longer lifetime of photogenerated electron-hole pairs, faster interfacial charge transfer rate with high surface area. A possible Z-scheme reaction mechanism and the photodegradation process are illustrated in Fig. 13. Under solar light irradiation, both WO_3 and Fe_2O_3 can be excited to photogenerated electrons (e^-) and holes (h^+).

Based on the results, we propose MB and RhB dyes photo degradation over WFG composite through separation and transfer of photo induced electrons at Fe_2O_3 and WO_3 interface heterojunction. The CB of WO_3 electrons transferred (photo generated) to the valence band (VB) of Fe_2O_3, and the residual holes within the VB WO_3 may either mediated or directly produce hydroxyl radicals (reaction with H_2O) to react with dyes (photooxidize). The photogenerated e^- from Fe_2O_3 also react with adsorbed O_2 to produce $O_2^{\bullet-}$ radicals, while only a few $O_2^{\bullet-}$ radicals could further react with H_2O to generate hydroxyl radicals ($^{\bullet}OH$). The close contact between WO_3, Fe_2O_3 nanoparticles and the both CB band of WO_3 and Fe_2O_3 electrons may trapped rGO sheets, extending the lifetime of charge carriers and suppressing the rate of recombination. Also, the photoinduced electrons on WO_3, Fe_2O_3 surface and the trapped electrons on rGO sheets induce redox reaction in the targeted organic pollutants. The reduced GO can act as a back bone (transfer the electron) of e^- and h^+ pair separation mechanism.

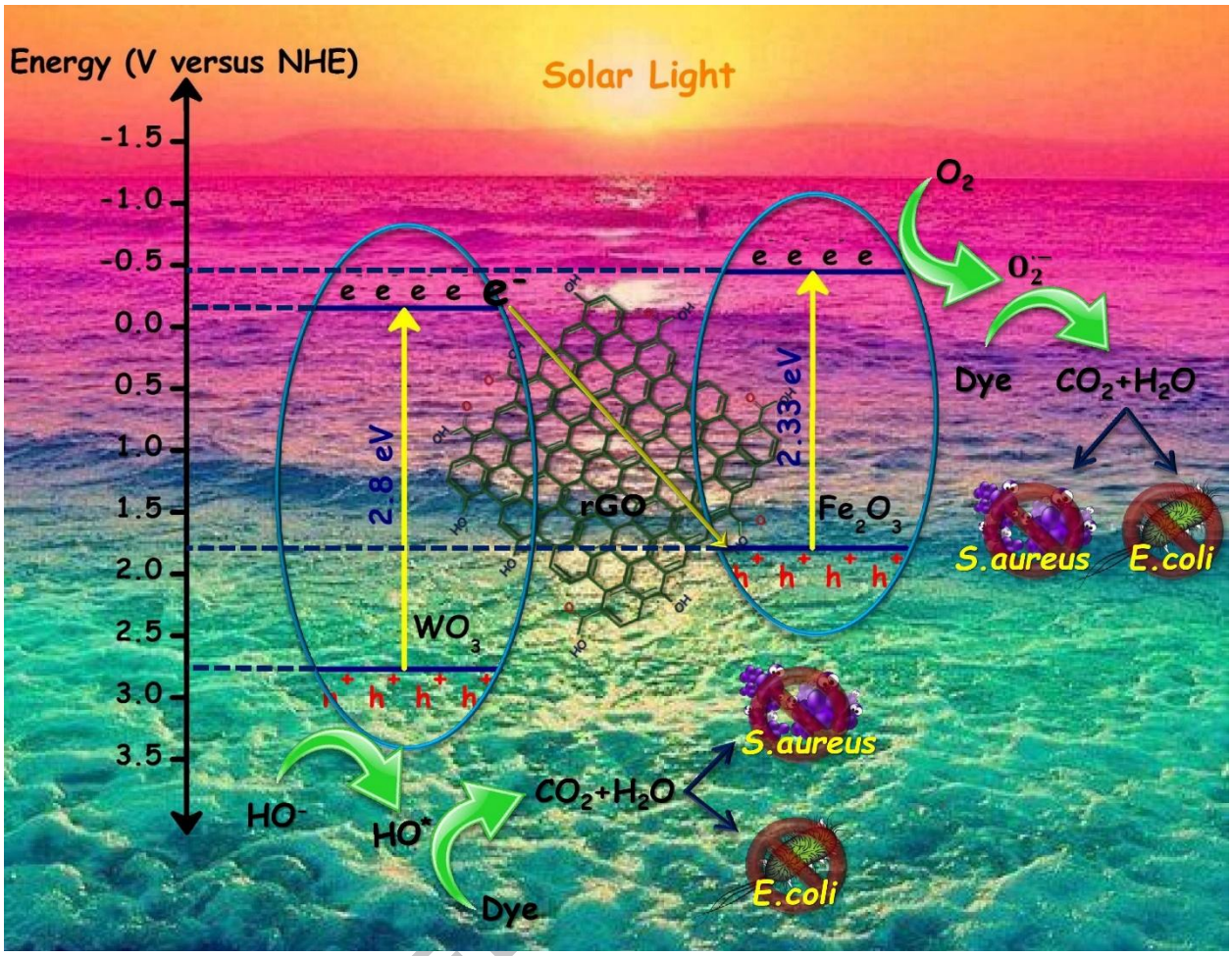

Fig. 13. Schematic diagram of proposed photodegradation z-scheme mechanism for WFG nanocomposites

3.6.2 Comparison with other reported systems

The efficiency of our photocatalyst was compared with other reports, as listed in Table 3. Notably the reports, used high lamp powers, low concentration of pollutants and removal efficiency is comparably lower than that of our report. It can be seen that our catalyst showed higher removal efficiency even high concentration dye within 20 min and less amount of catalyst as compared to the other reported system presented in Table 3.

Table 3. Comparison of solar light degradation rate (%) of MB over previously reported binary and ternary heterojunction

Catalyst	Dye	% Removal	Catalyst	Irradiation Time	Reference
WO_3/α-Fe_2O_3	MB	80	0.5 g/L	240	[20]
CeO_2/SnO_2/rGO	MB	95	0.5 g/L	90	[22]
Ag/RGO/ZnO	RhB	80	0.2 g/L	60	[31]
g-C_3N_4/Fe_3O_4/BiOI	RhB	97	0.1 g/L	180	[68]
TiO_2-RGO/MoS_2	MB	97	0.5 g/L	100	[69]
WO_3/Fe_2O_3/rGO	MB	98	0.1 g/L	20	Present work
WO_3/Fe_2O_3/rGO	RhB	94	0.1 g/L	20	Present work

3.7 Removal of toxic heavy metal ions

The selective Pb^{2+}, Cd^{2+} and Hg^{2+} metal ions removal efficiency of the prepared WFG nanocomposites was investigated with different pH (2-7), and the obtained results are presented in Fig. 12. From the results it is noted that the solution pH value strongly affected the heavy metal ions removal efficiency on the prepared WFG nanocomposites and removal percentage increases with increasing pH. The maximum removal percentage were recorded at the pH 6 for each metal ion (Pb^{2+} (76%), Cd^{2+} (81%) and Hg^{2+} (79%) with removal capacities of 229.2, 244.1, and 236.9 ppm, respectively. The adsorption capacity of WFG nanocomposites to the cadmium ion is higher than that of the lead and mercury ions. It seems to us that adsorption tendency of the ions is also possibly dependent on the size/softness of ion species as well. It should be noted that the removal percentage of WFG nanocomposites is very low at initial pH from 2 to 4 [70], however, further increase in pH from 5 to 6 there is remarkable change in removal capacity of WFG nanocomposites was observed. Moreover, abundant of H^+ ions in this solution could compete with metal ions for available adsorption sites on WFG nanocomposites. However, WFG

nanocomposites became negative charge due to the deprotonation surface when pH > 5-6 which could be responsible for the maximum removal capacity.

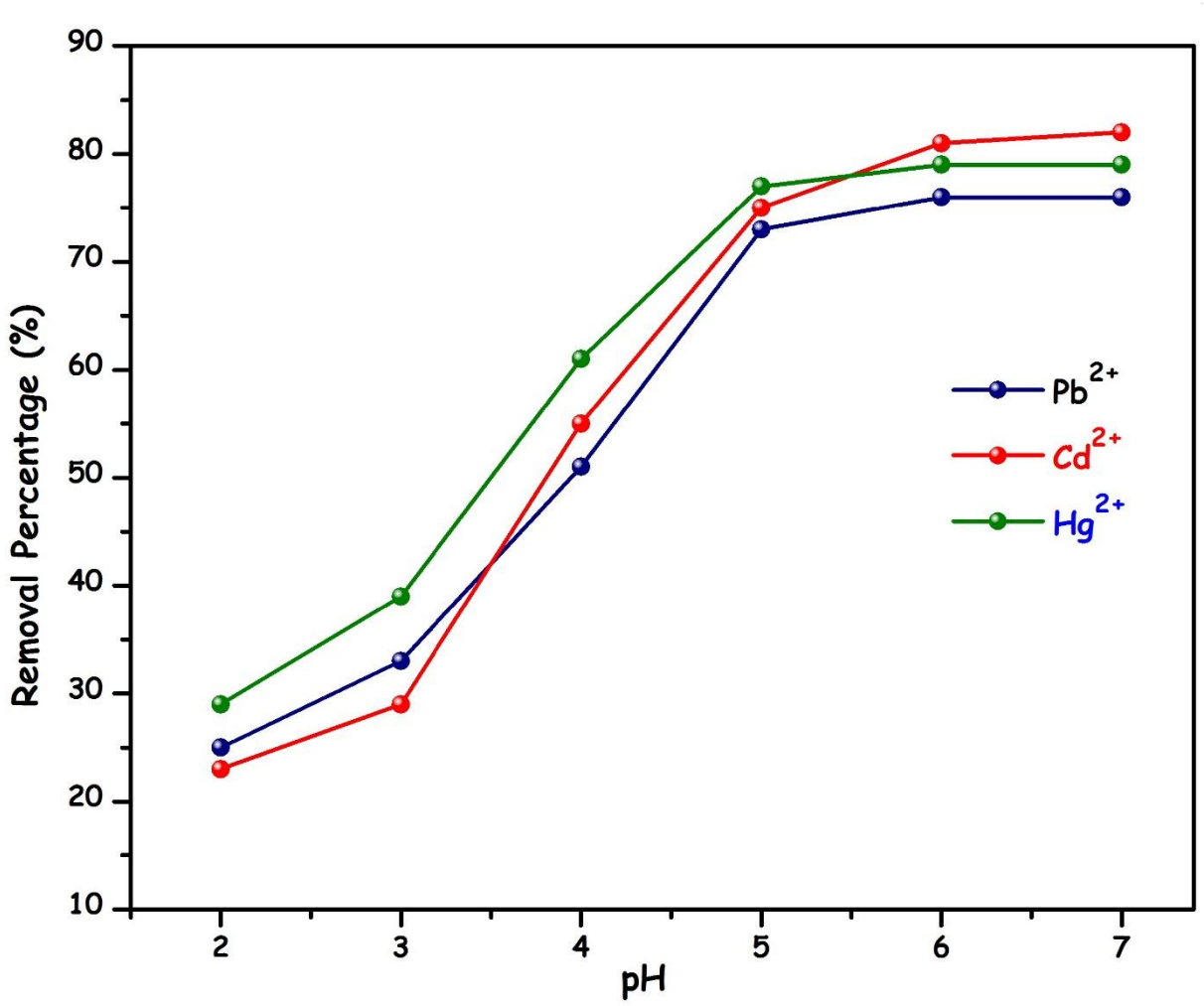

Fig. 14. pH dependence of the metal ions removal by the WFG ternary nanocomposite

3.8 Antibacterial Activity

The present study analyzed the antibacterial effects of WFG ternary nanocomposite against two pathogenic bacteria name called *E. coli* and *S. aureus*. Fig. 15. showed the zone of inhibition around the bacterial strain for WFG nanocomposite. Both bacterial organisms are most common in enteric infections, water pollution and resistance to most broad spectrum of new

generation antibiotics. In addition, nanocomposites damaged the cellular function by denaturation of cell enzymes, biological molecules and protein factors [71]. The as prepared WFG nanocomposite has been screened *in vitro* antibacterial activity on selected Gram negative *E. coli* and Gram positive bacteria *S. aureus* at different concentrations. The results are summarised in Table 4. WFG nanocomposite showed much higher antibacterial activity compared to both pure and binary composites (Fig. 15.). Decrease in the antibacterial efficacy in the prepared nanocomposite against *E. coli* may be due its gram negative nature. It is well known that gram negative bacteria consist of multiple cell walls compared to gram positive bacteria (*S. aureus*). From this study, it is evident that the cells exposed to WFG photocatalysis, have improved antibacterial activities, due to active oxygen species from the metal oxide nanocomposites.

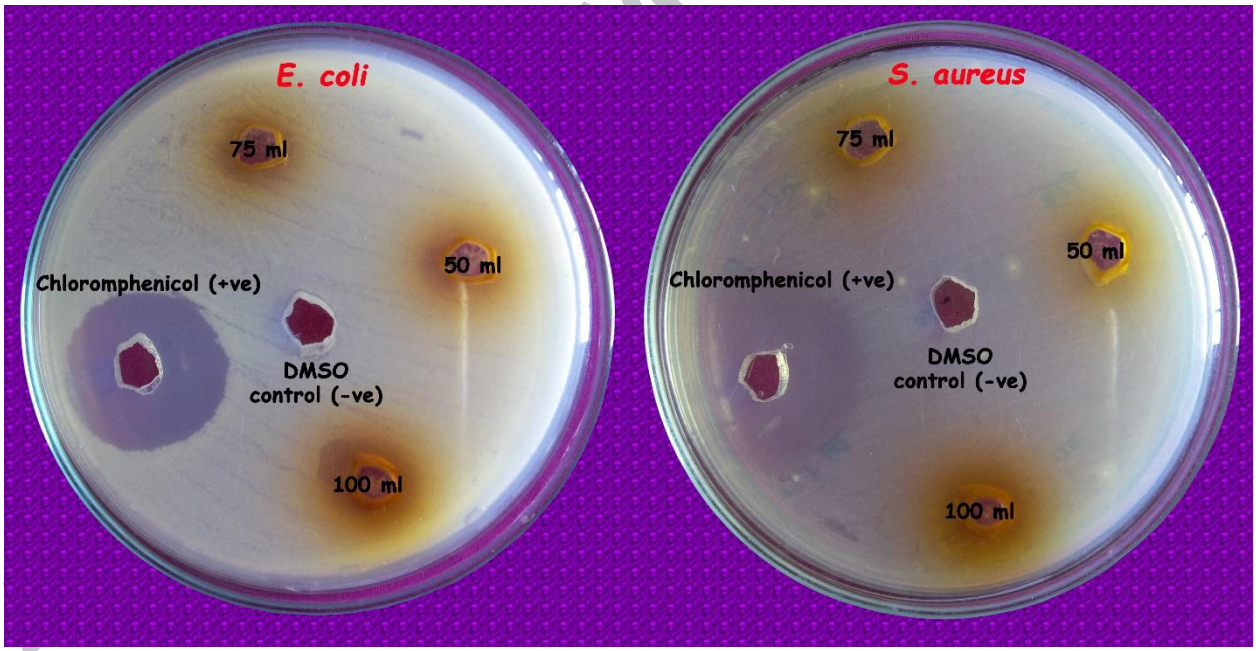

Fig. 15. Zone of inhibition tests for WFG nanocomposites materials towards gram-negative *E. coli* bacteria and gram-positive *S. aureus* bacteria

Table. 4. Antibacterial activity of the catalysts against two human pathogenic bacteria

Nanocomposites	Bacterial strain used	Zone of inhibition level (in mm) (Mean value of four measurements)			Standard 3 µl
		50 µg	75 µg	100 µg	
WFG	*E. coli*	10.4±1.2	12.3±3.5	15.6±1.4	35.00±2.0
	S. aureus	12.2±1.4	14.5±2.4	19.3±1.2	35.23±1.6

4. Conclusion

In summary, we have showed the successful synthesis of WO_3-Fe_2O_3-rGO ternary nanocomposites via a simple hydrothermal method with good photostability and recyclability. The resultant WFG nanocomposites deliver more adsorption and reaction sites, positively shift the position of the valence band potential and enhance charge transportation and separation efficiency. WFG nanocomposites show better photocatalytic activity for MB and RhB dyes under solar light irradiation, which is higher than pure and binary nanocomposites. The removal of heavy metal ions from the water has been successfully carried out by respective adsorption, photoreduction and photooxidation. Furthermore, WFG nanocomposites showed the considerable antibacterial performance and could be possibly used to treat domestic wastewater. In this report, provide new inroads into exploration and utilization of graphene-based nanocomposites with efficient performance in purifying polluted water resources.

References

[1] P. Dong, G. Hou, X. Xi, R. Shao, F. Dong, WO_3 -based photocatalysts: morphology control, activity enhancement and multifunctional applications, Environ. Sci. Nano. 4 (2017) 539–557. doi:10.1039/C6EN00478D.

[2] M.D. Hernando, S. De Vettori, M.J. Martínez Bueno, A.R. Fernández-Alba, Toxicity evaluation with Vibrio fischeri test of organic chemicals used in aquaculture, Chemosphere. 68 (2007) 724–730. doi:10.1016/j.chemosphere.2006.12.097.

[3] V. Vasanthakumar, A. Priyadharsan, P.M. Anbarasan, S. Muthumari, S. Subramanian, V. Raj, Enhancing Toxic Metal Ions and Dye Removal Properties of Nanostructured Terpolymer Formed by Diaminodiphenylmethane-Resorcinol-Formaldehyde, ChemistrySelect. 2 (2017) 9501–9510. doi:10.1002/slct.201700685.

[4] K. Vinodgopal, D.E. Wynkoop, P. V. Kamat, Environmental photochemistry on semiconductor surfaces: Photosensitized degradation of a textile azo dye, Acid Orange 7, on TiO_2 particles using visible light, Environ. Sci. Technol. 30 (1996) 1660–1666. doi:10.1021/es950655d.

[5] S. Masudy-Panah, R. Siavash Moakhar, C.S. Chua, H.R. Tan, T.I. Wong, D. Chi, G.K. Dalapati, Nanocrystal Engineering of Sputter-Grown CuO Photocathode for Visible-Light-Driven Electrochemical Water Splitting, ACS Appl. Mater. Interfaces. 8 (2016) 1206–1213. doi:10.1021/acsami.5b09613.

[6] O. Hamdaoui, Intensification of the sorption of Rhodamine B from aqueous phase by loquat seeds using ultrasound, Desalination. 271 (2011) 279–286. doi:10.1016/j.desal.2010.12.043.

[7] V. Krishnakumar, R. Ranjith, J. Jayaprakash, S. Boobas, J. Venkatesan, Enhancement of

photocatalytic degradation of methylene blue under visible light using transparent Mg-doped CdS–PVA nanocomposite films, J. Mater. Sci. Mater. Electron. 28 (2017) 13990–13999. doi:10.1007/s10854-017-7249-z.

[8] T. Torimoto, Y. Kamiya, T. Kameyama, H. Nishi, T. Uematsu, S. Kuwabata, T. Shibayama, Controlling Shape Anisotropy of ZnS-$AgInS_2$ Solid Solution Nanoparticles for Improving Photocatalytic Activity, ACS Appl. Mater. Interfaces. 8 (2016) 27151–27161. doi:10.1021/acsami.6b10408.

[9] S. Shanavas, A. Priyadharsan, V. Vasanthakumar, A. Arunkumar, P.M. Anbarasan, S. Bharathkumar, Mechanistic investigation of visible light driven novel La_2CuO_4/CeO_2/rGO ternary hybrid nanocomposites for enhanced photocatalytic performance and antibacterial activity, J. Photochem. Photobiol. A Chem. 340 (2017) 96–108. doi:10.1016/j.jphotochem.2017.03.002.

[10] V. Vasanthakumar, A. Saranya, A. Raja, S. Prakash, V. Anbarasu, P. Priya, V. Raj, The synthesis, characterization, removal of toxic metal ions and: In vitro biological applications of a sulfanilamide-salicylic acid-formaldehyde terpolymer, RSC Adv. 6 (2016). doi:10.1039/c6ra05115d.

[11] A. Halder, S. Patra, B. Viswanath, N. Munichandraiah, N. Ravishankar, Porous, catalytically active palladium nanostructures by tuning nanoparticle interactions in an organic medium, Nanoscale. 3 (2011) 725–730. doi:10.1039/C0NR00640H.

[12] A.P. Alivisatos, K.P. Johnsson, X. Peng, T.E. Wilson, C.J. Loweth, M.P. Bruchez, P.G. Schultz, Organization of'nanocrystal molecules' using DNA, Nature. 382 (1996) 609–11. doi:10.1038/382609a0.

[13] A. Fakhri, S. Behrouz, Photocatalytic properties of tungsten trioxide (WO_3) nanoparticles

for degradation of Lidocaine under visible and sunlight irradiation, Sol. Energy. 112 (2015) 163–168. doi:10.1016/j.solener.2014.11.014.

[14] D. Bi, Y. Xu, Improved Photocatalytic Activity of WO3through Clustered Fe_2O_3 for Organic Degradation in the Presence of H_2O_2, Langmuir. 27 (2011) 9359–9366. doi:10.1021/la2012793.

[15] W. Sun, Q. Meng, L. Jing, D. Liu, Y. Cao, Facile synthesis of surface-modified nanosized α-Fe_2O_3 as efficient visible photocatalysts and mechanism insight, J. Phys. Chem. C. 117 (2013) 1358–1365. doi:10.1021/jp309599d.

[16] C. Diaz, L. Barrientos, D. Carrillo, J. Valdebenito, M.L. Valenzuela, P. Allende, H. Geaney, C. O'Dwyer, Solvent-less method for efficient photocatalytic α-Fe_2O_3 nanoparticles using macromolecular polymeric precursors, New J. Chem. 40 (2016) 6768–6776. doi:10.1039/C6NJ00561F.

[17] P. Basnet, G.K. Larsen, R.P. Jadeja, Y.-C. Hung, Y. Zhao, α-Fe_2O_3 Nanocolumns and Nanorods Fabricated by Electron Beam Evaporation for Visible Light Photocatalytic and Antimicrobial Applications, ACS Appl. Mater. Interfaces. 5 (2013) 2085–2095. doi:10.1021/am303017c.

[18] Z. Ai, Z. Gao, L. Zhang, W. He, J.J. Yin, Core–Shell Structure Dependent Reactivity of Fe@Fe_2O_3 Nanowires on Aerobic Degradation of 4-Chlorophenol, Environ. Sci. Technol. 47 (2013) 5344–5352. doi:10.1021/es4005202.

[19] A. Memar, C.M. Phan, M.O. Tade, Photocatalytic activity of WO_3/Fe_2O_3 nanocomposite photoanode, Int. J. Hydrogen Energy. 40 (2015) 8642–8649. doi:10.1016/j.ijhydene.2015.05.016.

[20] R. Lei, H. Ni, R. Chen, B. Zhang, W. Zhan, Y. Li, Hydrothermal synthesis of WO_3/Fe_2O_3

nanosheet arrays on iron foil for photocatalytic degradation of methylene blue, J. Mater. Sci. Mater. Electron. (2017) 1–7.

[21] L. Yin, D.L. Chen, M.J. Feng, L.F. Ge, D.W. Yang, Z.H. Song, B.B. Fan, R. Zhang, G.S. Shao, Hierarchical Fe_2O_3@WO_3 nanostructures with ultrahigh specific surface areas: microwave-assisted synthesis and enhanced H_2S-sensing performance, Rsc Adv. 5 (2015) 328–337. doi:10.1039/c4ra10500a.

[22] A. Priyadharsan, V. Vasanthakumar, S. Karthikeyan, V. Raj, S. Shanavas, P.M. Anbarasan, Multi-functional properties of ternary CeO_2/SnO_2/rGO nanocomposites: Visible light driven photocatalyst and heavy metal removal, J. Photochem. Photobiol. A Chem. 346 (2017) 32–45. doi:10.1016/j.jphotochem.2017.05.030.

[23] F. Li, B. Dong, Construction of novel Z-scheme Cu_2O/graphene/α-Fe_2O_3 nanotube arrays composite for enhanced photocatalytic activity, Ceram. Int. 43 (2017) 1–6. doi:10.1016/j.ceramint.2017.08.021.

[24] J. Guo, Y. Li, S. Zhu, Z. Chen, Q. Liu, D. Zhang, W.-J. Moon, D.-M. Song, Synthesis of WO_3@Graphene composite for enhanced photocatalytic oxygen evolution from water, RSC Adv. 2 (2012) 1356. doi:10.1039/c1ra00621e.

[25] H. Li, Q. Zhao, X. Li, Z. Zhu, M. Tade, S. Liu, Fabrication, characterization, and photocatalytic property of α-Fe_2O_3/graphene oxide composite, J. Nanoparticle Res. 15 (2013). doi:10.1007/s11051-013-1670-x.

[26] A. Cordero-GarcÃ-a, J.L. GuzmÃ¡n-Mar, L. Hinojosa-Reyes, E. Ruiz-Ruiz, A. HernÃ¡ndez-RamÃ-rez, Effect of carbon doping on WO_3/TiO_2 coupled oxide and its photocatalytic activity on diclofenac degradation, Ceram. Int. 42 (2016) 9796–9803. doi:10.1016/j.ceramint.2016.03.073.

[27] W. Wan, S. Yu, F. Dong, Q. Zhang, Y. Zhou, Efficient C_3N_4/graphene oxide macroscopic aerogel visible-light photocatalyst, J. Mater. Chem. A. 4 (2016) 7823–7829. doi:10.1039/C6TA01804A.

[28] R. Zhang, M. Ma, Q. Zhang, F. Dong, Y. Zhou, Multifunctional g-C_3N_4/graphene oxide wrapped sponge monoliths as highly efficient adsorbent and photocatalyst, Appl. Catal. B Environ. 235 (2018) 17–25. doi:10.1016/j.apcatb.2018.04.061.

[29] J. Low, J. Yu, W. Ho, Graphene-Based Photocatalysts for CO_2 Reduction to Solar Fuel, J. Phys. Chem. Lett. 6 (2015) 4244–4251. doi:10.1021/acs.jpclett.5b01610.

[30] A.R. Nanakkal, L.K. Alexander, Graphene/$BiVO_4$/TiO_2 nanocomposite: tuning band gap energies for superior photocatalytic activity under visible light, J. Mater. Sci. 52 (2017) 7997–8006. doi:10.1007/s10853-017-1002-0.

[31] D.K. Surendran, M.M. Xavier, V.P. Viswanathan, S. Mathew, Synthesis of a ternary Ag/RGO/ZnO nanocomposite via microwave irradiation and its application for the degradation of Rhodamine B under visible light, Environ. Sci. Pollut. Res. 24 (2017) 15360–15368. doi:10.1007/s11356-017-9135-x.

[32] K. Sharma, K. Maiti, N.H. Kim, D. Hui, J.H. Lee, Green synthesis of glucose-reduced graphene oxide supported Ag-Cu_2O nanocomposites for the enhanced visible-light photocatalytic activity, Compos. Part B Eng. 138 (2018) 35–44. doi:10.1016/j.compositesb.2017.11.021.

[33] A. Kumar, L. Rout, L.S.K. Achary, S.K. Mohanty, P. Dash, A combustion synthesis route for magnetically separable graphene oxide–$CuFe_2O_4$–ZnO nanocomposites with enhanced solar light-mediated photocatalytic activity, New J. Chem. 41 (2017) 10568–10583. doi:10.1039/C7NJ02070H.

[34] M.P. Doyle, F. Busta, B.R. Cords, P.M. Davidson, J. Hawke, H.S. Hurd, R.E. Isaacson, K. Matthews, J. Maurer, J. Meng, T.J. Montville, T.R. Shryock, J.N. Sofos, A.K. Vidaver, L. Vogel, Antimicrobial resistance: Implications for the food system: An expert report, funded by the IFT Foundation, Compr. Rev. Food Sci. Food Saf. 5 (2006) 71–137. doi:10.1111/j.1541-4337.2006.00004.x.

[35] Q. Li, S. Mahendra, D. Lyon, L. Brunet, M. Liga, Antimicrobial nanomaterials for water disinfection and microbial control: potential applications and implications, Water Res. (n.d.). http://www.sciencedirect.com/science/article/pii/S0043135408003333.

[36] R. Gupta, N.K. Eswar, J.M. Modak, G. Madras, Effect of morphology of zinc oxide in ZnO-CdS-Ag ternary nanocomposite towards photocatalytic inactivation of E. coli under UV and visible light, Chem. Eng. J. 307 (2017) 966–980. doi:10.1016/j.cej.2016.08.142.

[37] B. Ahmed, A.K. Ojha, F. Hirsch, I. Fischer, D. Patrice, A. Materny, Tailoring of enhanced interfacial polarization in WO_3 nanorods grown over reduced graphene oxide synthesized by a one-step hydrothermal method, RSC Adv. 7 (2017) 13985–13996. doi:10.1039/C7RA00730B.

[38] H. Yang, L. Sun, J. Zhai, H. Li, Y. Zhao, H. Yu, In situ controllable synthesis of magnetic Prussian blue/graphene oxide nanocomposites for removal of radioactive cesium in water, J. Mater. Chem. A. 2 (2014) 326–332. doi:10.1039/C3TA13548A.

[39] W. Qian, R. Hao, Y. Hou, Y. Tian, C. Shen, H. Gao, X. Liang, Solvothermal-assisted exfoliation process to produce graphene with high yield and high quality, Nano Res. 2 (2009) 706–712. doi:10.1007/s12274-009-9074-z.

[40] X. Zhong, Y. Feng, W. Knoll, M. Han, Alloyed $Zn_xCd_{1-x}S$ Nanocrystals with Highly Narrow Luminescence Spectral Width, J. Am. Chem. Soc. 125 (2003) 13559–13563.

doi:10.1021/ja036683a.

[41] S. Singh, N. Khare, Reduced graphene oxide coupled CdS/$CoFe_2O_4$ ternary nanohybrid with enhanced photocatalytic activity and stability: a potential role of reduced graphene oxide as a visible light responsive photosensitizer, RSC Adv. 5 (2015) 96562–96572. doi:10.1039/c5ra14889h.

[42] Z. Bo, X. Shuai, S. Mao, H. Yang, J. Qian, J. Chen, J. Yan, K. Cen, Green preparation of reduced graphene oxide for sensing and energy storage applications, Sci. Rep. 4 (2014). doi:10.1038/srep04684.

[43] S. Shanavas, A. Priyadharsan, R. Ramesh, P.M. Anbarasan, Optimization and Detailed Stability Study on Pb Doped Ceria Nanocubes for Enhanced Photodegradation of Several Anionic and Cationic Organic Pollutants, Arab. J. Chem. (2017). doi:10.1016/j.arabjc.2017.11.001.

[44] B. Li, T. Liu, Y. Wang, Z. Wang, ZnO/graphene-oxide nanocomposite with remarkably enhanced visible-light-driven photocatalytic performance, J. Colloid Interface Sci. 377 (2012) 114–121. doi:10.1016/j.jcis.2012.03.060.

[45] G. Mishra, G.C. Behera, S.K. Singh, K.M. Parida, Liquid phase esterification of acetic acid over WO_3 promoted β-SiC in a solvent free system, Dalt. Trans. 41 (2012) 14299. doi:10.1039/c2dt31468a.

[46] M.M. Rahman, A.M. Asiri, Development of ionic-sensor based on sono-chemically prepared low-dimensional β-Fe_2O_3 nanoparticles onto flat-gold electrodes by an electrochemical approach, Sens. Bio-Sensing Res. 4 (2015) 109–117. doi:10.1016/j.sbsr.2015.05.001.

[47] M. Dou, M. Hou, H. Zhang, G. Li, W. Lu, Z. Wei, Z. Shao, B. Yi, A highly stable anode,

carbon-free, catalyst support based on tungsten trioxide nanoclusters for proton-exchange membrane fuel cells, ChemSusChem. 5 (2012) 945–951. doi:10.1002/cssc.201100706.

[48] et al. Vuong, N.M., Porous Au- embedded WO_3 nanowire structure for efficient detection of CH_4 and H_2S, (2015).

[49] M. Vasilopoulou, A. Soultati, D.G. Georgiadou, T. Stergiopoulos, L.C. Palilis, S. Kennou, N.A. Stathopoulos, D. Davazoglou, P. Argitis, Hydrogenated under-stoichiometric tungsten oxide anode interlayers for efficient and stable organic photovoltaics, J. Mater. Chem. A. 2 (2014) 1738–1749. doi:10.1039/c3ta13975a.

[50] L. Yin, D. Chen, M. Feng, L. Ge, D. Yang, Z. Song, B. Fan, R. Zhang, G. Shao, Hierarchical Fe_2O_3@WO_3 nanostructures with ultrahigh specific surface areas: Microwave-assisted synthesis and enhanced H_2S-sensing performance, RSC Adv. 5 (2015) 328–337. doi:10.1039/c4ra10500a.

[51] G.K. Pradhan, D.K. Padhi, K.M. Parida, Fabrication of α-Fe_2O_3 Nanorod/RGO composite: A novel hybrid photocatalyst for phenol degradation, ACS Appl. Mater. Interfaces. 5 (2013) 9101–9110. doi:10.1021/am402487h.

[52] F. Kayaci, S. Vempati, C. Ozgit-Akgun, I. Donmez, N. Biyikli, T. Uyar, Selective isolation of the electron or hole in photocatalysis: ZnO-TiO_2 and TiO_2-ZnO core-shell structured heterojunction nanofibers via electrospinning and atomic layer deposition, Nanoscale. 6 (2014) 5735–5745. doi:10.1039/c3nr06665g.

[53] W.K. Jo, S. Kumar, M.A. Isaacs, A.F. Lee, S. Karthikeyan, Cobalt promoted TiO_2/GO for the photocatalytic degradation of oxytetracycline and Congo Red, Appl. Catal. B Environ. 201 (2017) 159–168. doi:10.1016/j.apcatb.2016.08.022.

[54] H. Tang, G.J. Ehlert, Y. Lin, H.A. Sodano, Highly Efficient Synthesis of Graphene

Nanocomposites, Nanol. 12 (2011) 84.

[55] K. Thummavichai, L. Trimby, N. Wang, C.D. Wright, Y. Xia, Y. Zhu, Low Temperature Annealing Improves the Electrochromic and Degradation Behavior of Tungsten Oxide (WO_x) Thin Films, J. Phys. Chem. C. 121 (2017) 20498–20506. doi:10.1021/acs.jpcc.7b06300.

[56] B. Zhao, X. Xu, J. Gao, Q. Fu, Y. Tang, Structure characterization of WO_3/ZrO_2 catalysts by Raman spectroscopy, J. Raman Spectrosc. 27 (1996). doi:10.1002/(SICI)1097-4555(199607)27:7<549::AID-JRS1>3.0.CO;2-9.

[57] D. Bersani, P.P. Lottici, A. Montenero, Micro-Raman investigation of iron oxide films and powders produced by sol-gel syntheses, J. Raman Spectrosc. 30 (1999) 355–360. doi:10.1002/(SICI)1097-4555(199905)30:5<355::AID-JRS398>3.0.CO;2-C.

[58] K. Rout, M. Mohapatra, S. Layek, A. Dash, H.C. Verma, S. Anand, The influence of precursors on phase evolution of nano iron oxides/oxyhydroxides: Optical and magnetic properties, New J. Chem. 38 (2014) 3492–3506. doi:10.1039/c4nj00526k.

[59] X. Liu, Y. Nie, H. Yang, S. Sun, Y. Chen, T. Yang, S. Lin, Enhancement of the photocatalytic activity and electrochemical property of graphene-$SrWO_4$ nanocomposite, Solid State Sci. 55 (2016) 130–137. doi:10.1016/j.solidstatesciences.2016.03.006.

[60] L. Peng, T. Xie, Y. Lu, H. Fan, D. Wang, Synthesis, photoelectric properties and photocatalytic activity of the Fe_2O_3/TiO_2 heterogeneous photocatalysts, Phys. Chem. Chem. Phys. 12 (2010) 8033. doi:10.1039/c002460k.

[61] L. Zhang, Z. Bao, X. Yu, P. Dai, J. Zhu, M. Wu, G. Li, X. Liu, Z. Sun, C. Chen, Rational Design of α-Fe_2O_3/Reduced Graphene Oxide Composites: Rapid Detection and Effective Removal of Organic Pollutants, ACS Appl. Mater. Interfaces. 8 (2016) 6431–6438.

doi:10.1021/acsami.5b11292.

[62] K. Ramar, V. Vasanthakumar, A. Priyadharsan, P. Priya, V. Raj, P.M. Anbarasan, R. Vasanthakumari, A. Jafar Ahamed, Green synthetic approach of silver nanoparticles from Bauhinia tomentosa Linn. leaves extract for potent photocatalytic and in vitro biological applications, J. Mater. Sci. Mater. Electron. (2018). doi:10.1007/s10854-018-9246-2.

[63] R. Ameta, M.S. Solanki, S. Benjamin, S.C. Ameta, Photocatalysis, in: Adv. Oxid. Process. Waste Water Treat., Elsevier, 2018: pp. 135–175. doi:10.1016/B978-0-12-810499-6.00006-1.

[64] H. Wu, S. Lin, C. Chen, W. Liang, X. Liu, H. Yang, A new ZnO/rGO/polyaniline ternary nanocomposite as photocatalyst with improved photocatalytic activity, Mater. Res. Bull. 83 (2016) 434–441. doi:10.1016/j.materresbull.2016.06.036.

[65] S. Karthikeyan, D.D. Dionysiou, A.F. Lee, S. Suvitha, P. Maharaja, K. Wilson, G. Sekaran, Hydroxyl radical generation by cactus-like copper oxide nanoporous carbon catalysts for microcystin-LR environmental remediation, Catal. Sci. & Technol. (2016). doi:10.1039/c5cy00888c.

[66] S. Karthikeyan, G. Sekaran, In situ generation of a hydroxyl radical by nanoporous activated carbon derived from rice husk for environmental applications: Kinetic and thermodynamic constants, Phys. Chem. Chem. Phys. 16 (2014) 3924–3933. doi:10.1039/c3cp54185a.

[67] R. Rajendran, K. Varadharajan, V. Jayaraman, B. Singaram, J. Jeyaram, Photocatalytic degradation of metronidazole and methylene blue by PVA-assisted Bi_2WO_6–CdS nanocomposite film under visible light irradiation, Appl. Nanosci. 8 (2018) 61–78. doi:10.1007/s13204-018-0652-9.

[68] R. Kumar, M.O. Ansari, N. Parveen, M. Oves, M.A. Barakat, A. Alshahri, M.Y. Khan, M.H. Cho, Facile route to a conducting ternary polyaniline@TiO_2/GN nanocomposite for environmentally benign applications: photocatalytic degradation of pollutants and biological activity, RSC Adv. 6 (2016) 111308–111317. doi:10.1039/C6RA24079H.

[69] D.B. Nimbalkar, H.-H. Lo, P.V.R.K. Ramacharyulu, S.-C. Ke, Improved photocatalytic activity of RGO/MoS_2 nanosheets decorated on TiO_2 nanoparticles, RSC Adv. 6 (2016) 31661–31667. doi:10.1039/C6RA01591C.

[70] V. Vasanthakumar, A. Saranya, A. Raja, S. Prakash, V. Anbarasu, P. Priya, V. Raj, The synthesis, characterization, removal of toxic metal ions and in vitro biological applications of a sulfanilamide–salicylic acid–formaldehyde terpolymer, RSC Adv. 6 (2016) 54904–54917. doi:10.1039/C6RA05115D.

[71] S. Vignesh, A.L. Muppudathi, J.K. Sundar, Multifunctional performance of gC_3N_4-$BiFeO_3$-Cu_2O hybrid nanocomposites for magnetic separable photocatalytic and antibacterial activity, J. Mater. Sci. Mater. Electron. (2018). doi:10.1007/s10854-018-9144-7.

Graphical Abstract

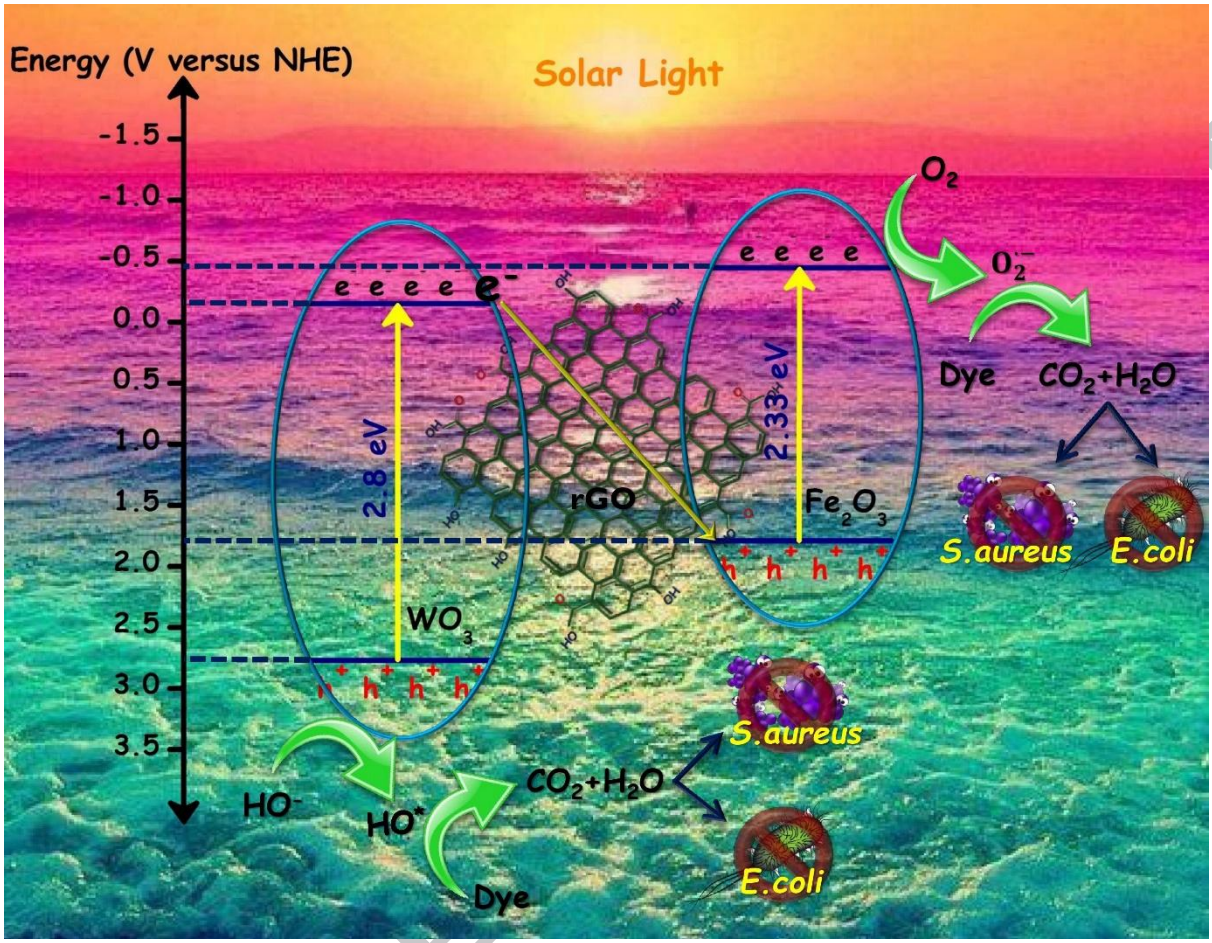

Highlights

- The effect of rGO based WO_3 and Fe_2O_3 ternary nanocomposite was extensively investigated.
- rGO in ternary nanocomposite could reduce the recombination of electron hole pairs.
- The as-prepared ternary nanocomposites showed enhanced photocatalytic activity, metal ion removal and antibacterial activity.
- Mechanism of enhanced photocatalytic activity was proposed and discussed.